Resistivity modeling for arbitrarily shaped three-dimensional structures

A. Dey* and H. F. Morrison‡

A numerical technique has been developed to solve the three-dimensional (3-D) potential distribution about a point source of current located in or on the surface of a half-space containing an arbitrary 3-D conductivity distribution. Self-adjoint difference equations are obtained for Poisson's equation using finite-difference approximations in conjunction with an elemental volume discretization of the lower half-space. Potential distribution at all points in the set defining the subsurface are simultaneously solved for multiple point sources of current. Accurate and stable solutions are obtained using full, banded, Cholesky decomposition of the capacitance matrix as well as the recently developed incomplete Cholesky-conjugate gradient iterative method.

A comparison of the 2-D and 3-D simple block-shaped models, for the collinear dipole-dipole array, indicates substantially lower anomaly indices for inhomogeneities of finite strike-extent. In general, the strike-extents of inhomogeneities have to be approximately 10 times the dipole lengths before the response becomes 2-D. The saturation effect with increasing conductivity contrasts appears sooner for the 3-D conductive inhomogeneities than for corresponding models with infinite strike-lengths.

A downhole-to-surface configuration of electrodes produces diagnostic total field apparent resistivity maps for 3-D buried inhomogeneities. Experiments with various lateral and depth locations of the current pole indicate that mise-à-la-masse surveys give the largest anomaly if a current pole is located asymmetrically and, preferably, near the top surface of the buried conductor.

INTRODUCTION

Full utilization of the electrical resistivity method in geophysical prospecting has been limited by an inability to calculate the anomalies caused by specific structures. The widespread application of the dc resistivity and induced-polarization methods as primary exploration tools, coupled with developments in rapid, accurate, data acquisition techniques, warrant more quantitative interpretation of the geologic structure than is currently practiced. In the past decade, substantial advances have been made in this direction through analog and numerical modeling techniques for 2-D geologic structures (e.g., McPhar Geophysics, 1966; Madden, 1967; Coggon, 1971; Lee, 1975; Jepsen, 1969; Mufti, 1976; Dey and Morrison, 1976). In complex geologic environments often encountered in geothermal and mineral exploration, however, even a 2-D portrayal of the structure is often

inadequate and more complex solutions for 3-D distribution of resistivity must be sought.

Several solutions have been presented for the resistivity response of 3-D structures. Some analog scale modeling (McPhar Geophysics, 1966) has increased the understanding of the responses for a model suite of restricted physical dimensions and large conductivity contrasts. Numerical techniques using integral equation formulations have been developed by Dieter et al (1969) and Bakbak (1977) for a single body located in a conductive half-space, and by Hohmann (1975) and Meyer (1977) for a single rectangular, prismatic inhomogeneity situated in a half-space with or without an isotropic overburden layer of uniform thickness. These new techniques provide valuable information for the interpretation of data obtained in simple geologic situations involving a single, laterally bounded inhomogeneity. In practice,

however, the conductive targets occur as bodies of finite strike-length, variable dip, and in the vicinity of faults, beneath overburden of variable thickness and conductivity. It is necessary, therefore, to develop numerical modeling techniques to simulate structures with a totally arbitrary 3-D distribution of electrical conductivity.

A direct, explicit finite-difference technique is employed to solve for the potential distribution due to a point source of current in or on the surface of a half-space with an arbitrary 3-D distribution of conductivity. The finite-difference scheme is chosen because of the inherent simplicity of the approximation forms which are also easily amenable to Dirichlet, Neumann, or mixed-boundary conditions. Poisson's equation is discretized by elemental volumes over an irregularly spaced 3-D prismatic grid. The unknown potential at all of the nodes in the grid is evaluated by using successive overrelaxation, incomplete Cholesky-conjugate gradient, and direct matrix decomposition techniques to obtain accurate and stable solutions.

Using algebraic combinations of the potentials due to point current sources of opposite sign located inside or on the surface of the half-space, any arbitrary electrode configuration used in prospecting may be simulated. Results of certain surficial and downhole electrode configurations employed over a number of 3-D structures are illustrated later.

FUNDAMENTAL RELATIONS

Ohm's law relates the current density $\mathbf{J}$ to electric field intensity $\mathbf{E}$ and an isotropic conductivity σ by

$$\mathbf{J} = \sigma \mathbf{E}.$$

Since stationary electric fields are conservative,

$$\mathbf{E} = -\nabla \phi,$$

where ϕ is the electric potential.

Applying the principle of conservation of charge over a volume, and using the equation of continuity, we obtain

$$\nabla \cdot \mathbf{J} = (\partial \rho / \partial t)\, \delta(x)\, \delta(y)\, \delta(z), \tag{1}$$

where ρ is the charge density specified at a point in the cartesian x-y-z space by the Dirac delta function.

Equation (1) can be rewritten for a generalized 3-D space as

$$-\nabla \cdot [\sigma(x, y, z) \nabla \phi(x, y, z)] = (\partial \rho / \partial t) \cdot \\ \cdot \delta(x - x_s)\, \delta(y - y_s)\, \delta(z - z_s), \tag{2}$$

where (x_s, y_s, z_s) are the coordinates of the point source of injected charge.

Over an elemental volume ΔV about the charge injection point, the source term of equation (2) can be rewritten as

$$\partial \rho / \partial t\, \delta(x - x_s)\, \delta(y - y_s)\, \delta(z - z_s) \\ = (I / \Delta V)\, \delta(x - x_s)\, \delta(y - y_s)\, \delta(z - z_s),$$

where I is the current in amperes. Hence, equation (2) becomes

$$-\nabla \cdot [\sigma(x, y, z) \nabla \phi(x, y, z)] = (I / \Delta V) \cdot \\ \delta(x - x_s)\, \delta(y - y_s)\, \delta(z - z_s). \tag{3}$$

We will discuss methods for obtaining a numerical solution to equation (3) subject to the following boundary conditions: (1) $\phi(x, y, z)$ must be continuous across each boundary of the physical property distribution $\sigma(x, y, z)$, and (2) the normal component of $\mathbf{J} (\equiv \sigma \partial \phi / \partial \eta)$ must also be continuous across each boundary.

The solution of $\phi(x, y, z)$ is obtained by deriving the "difference equations" of (3) by a proper discretization of the (x, y, z) space over which the problem is to be solved.

Equation (3) is defined in a set $(x, y, z)\, \varepsilon R$, which is assumed to be closed and connected, to have a nonvoid interior and to have a sufficiently regular boundary Γ with outward normal η on which the boundary conditions are of the type

$$\alpha(x, y, z)\, \phi(x, y, z) + \beta(x, y, z) \frac{\partial \phi(x, y, z)}{\partial \eta} \\ = f_2(x, y, z),\ (x, y, z)\, \varepsilon R,$$

with

$$\alpha(x, y, z) \geq 0;\ \beta(x, y, z) \geq 0;\ (\alpha + \beta) > 0. \tag{4}$$

In physical simulation, we also have the conductivity distribution function that is at least piecewise continuous in R and its closure, and which satisfies $\sigma(x, y, z) > 0$, $(x, y, z) \varepsilon R$.

Equation (3) is a self-adjoint, strongly connected and nonseparable elliptic equation of second order (Varga, 1962). The procedure of finite-difference discretization solves, numerically, on a nonuniform rectangular prismatic mesh, the equation

$$L\phi(x, y, z) = -\nabla \cdot [\sigma(x, y, z) \nabla \phi(x, y, z)] \\ = \frac{I}{\Delta V} \delta(x - x_s)\, \delta(y - y_s) \cdot \\ \cdot \delta(z - z_s)$$
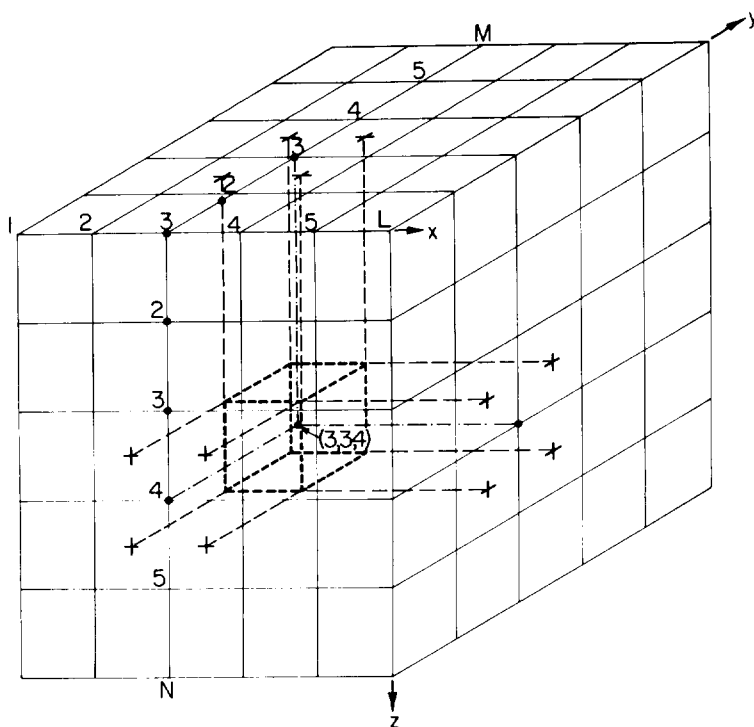
FIG. 1. 3-D discretization grid with rectangular cubic elements. The dotted lines show the elemental volume $\Delta V_{i,j,k}$ about a node (i, j, k).

on R, subject to the boundary condition (4). The positivity of $\sigma(x, y, z)$ implies that the operator L is positive definite.

DISCRETIZATION OF THE 3-D RESISTIVITY PROBLEM

To define the semiinfinite lower half-space with arbitrary conductivity distribution, the set R is designed with artificial boundaries simulating the *infinitely distant* planes in the horizontal (x- and y-directions) and the vertical (z-direction) extent. Such a lower half-space is illustrated by the grid shown in Figure 1. The grid is chosen to be a rectangular prism with arbitrary, irregular spacing of the nodes in the x-, y-, and z-directions. The nodes in the x-direction are indexed by $i = 1, 2, 3, \ldots, L$; those in the y-direction by $j = 1, 2, 3, \ldots, M$; and the nodes in the z-direction by $k = 1, 2, 3, \ldots, N$, respectively. The infinitely distant planes at $x = -\infty$ and $+\infty$ are represented by the nodes on the faces with $i = 1$ and L, respectively. Similarly, the infinitely distant planes at $y = -\infty$ and $+\infty$ are simulated by the nodes on the faces with $j = 1$ and

M, respectively, and the bottom plane at $z = \infty$ is represented by the face with $k = N$. The primary potential due to a point source on a half-space, as well as the secondary perturbational potentials due to conductivity inhomogeneities in the lower half-space, fall inversely with the radial distance away from the source. Hence, by assigning large numbers for L, M, and N with suitable coarsening of the grid as $i \to 1$, $i \to L$, $j \to 1$, $j \to M$, and $k \to N$ and appropriate boundary conditions, the infinitely distant planes could be simulated by a finite choice of L, M, and N.

BOUNDARY CONDITIONS APPLIED ON THE EDGE Γ OF THE REGION R

Since the simulation of the whole space is restricted to the conductive lower half-space alone in R, it is required that the boundary conditions be specified at points $(x, y, z)\Gamma \cup R$. At the ground surface with $z = 0$, this is implemented by applying the Neumann-type condition

$$\sigma_{i,j,k} \frac{\partial \phi_{i,j,k}}{\partial n} = 0,$$

for all $i = 1, 2, \ldots, L$; $j = 1, 2, 3, \ldots, M$ with $k = 1$.

The termination of the lower half-space at $x = \pm\infty$, $y = \pm\infty$, and $z = +\infty$ is done by extending the mesh far enough away from the sources and conductivity inhomogeneities that the total potential distribution at these planes approaches asymptotic values. The boundary values at these "infinitely distant planes" can be specified from known solutions of homogeneous or layered primary distribution of conductivity. Inhomogeneities are viewed as perturbations over this distribution. If these values are specified at all nodes on the infinitely distant planes, the boundary conditions on Γ become Dirichlet-type. In the general case of simulation of arbitrary conductivity distribution, often a suitable primary model solution cannot be analytically computed. In such cases, either (1) the total potential at these planes is assumed to be zero (Dirichlet condition) or (2) at these planes

$$\sigma_{i,j,k} \frac{\partial \phi_{i,j,k}}{\partial n}$$

is assumed to be zero (Neumann condition). It is often found that the first assumption causes an undershoot and the second assumption causes an overshoot in the numerically evaluated potentials beginning at some distance from the point source (Coggon, 1971) when compared with analytic solutions.

A mixed-boundary condition is proposed for the infinitely distant planes at $x = \pm\infty$, $y = \pm\infty$, and $z = \infty$, using the asymptotic behavior of $\phi(x, y, z)$ and $[\partial\phi(x, y, z)]/\partial n$ at large distances from the source point. The total potential at large distances from the source as well as inhomogeneities has the

general form of

$$\phi(x, y, z) \simeq \frac{A}{\sqrt{x^2 + y^2 + z^2}} = \frac{A}{r},$$

$$(A = \text{constant}).$$

Hence,

$$\frac{\partial \phi(x, y, z)}{\partial \eta} = -\frac{A}{r^2} \hat{e}_r \cdot \hat{\eta}$$

$$= -\frac{\phi(x, y, z)}{r} \cos\theta,$$

where θ is the angle between the radial distance r and the outward normal η. We can rewrite equation (4), therefore, as

$$\frac{\partial \phi(x, y, z)}{\partial \eta} + \frac{\alpha \phi(x, y, z)}{r} = 0 \qquad (5)$$

with

$$\alpha = \cos\theta.$$

Such a mixed-boundary condition takes advantage of the physical behavior of the potential at the distant bounding planes and does not require an a priori assumption of the nature of ϕ or $\partial\phi/\partial\eta$ that are to be evaluated in terms of a primary conductivity structure. It also has the inherent advantage of reducing the amount of coarsening of the grid required as the bounding planes are approached, and reflections due to the virtual sources along the edge nodes are simultaneously eliminated.

Discretization by elemental volume

The physical property distribution $\sigma_{i,j,k}$ at any node (i, j, k) of the prismatic grid (as shown in Figure 1) is discretized such that $\sigma_{i,j,k}$ represents the conductivity of a volume enclosed by the nodes $i, j, k; i+1, j, k; i, j+1, k; i+1, j+1, k; i, j, k+1; i+1, j, k+1; i, j+1, k+1;$ and $i+1, j+1, k+1$. The numerical solution of equation (3), that consists of a discretized set of $\phi_{i,j,k}$ at each node, is to be evaluated. The node (i, j, k) is assumed to represent the closed mesh region $\Delta V_{i,j,k}$ about the node as shown in Figure 1. It is seen that for a nodal point in the interior,

$$\Delta V_{i,j,k} = \frac{(\Delta x_i + \Delta x_{i-1}) \cdot (\Delta y_j + \Delta y_{j-1}) \cdot (\Delta z_k + \Delta z_{k-1})}{8},$$

and in the limit as $z \to 0$, for a nodal point on the ground surface,

$$\Delta V_{i,j,k} = \frac{(\Delta x_i + \Delta x_{i-1}) \cdot (\Delta y_j + \Delta y_{j-1}) \cdot \Delta z_k}{8}.$$

For each node (i, j, k) for which $\phi_{i,j,k}$ is unknown, we now integrate equation (3) over the corresponding elemental volume $\Delta V_{i,j,k}$ to obtain

$$-\iiint_{\Delta V_{i,j,k}} \nabla \cdot [\sigma(x, y, z) \nabla \phi(x, y, z)] dx_i dy_j dz_k$$

$$= \iiint_{\Delta V_{i,j,k}} \frac{I}{\Delta V_{i,j,k}} \cdot \delta(x_i - x_s)\,\delta(y_j - y_s) \cdot$$
$$\cdot \delta(z_k - z_s)\,dx_i\,dy_j\,dz_k$$
$$= I(x_s, y_s, z_s). \tag{6}$$

Using Green's theorem, the volume integral becomes

$$\iiint_{\Delta V_{i,j,k}} \nabla \cdot (\sigma \nabla \phi)\,dv = \iint_{S_{i,j,k}} \sigma \frac{\partial \phi}{\partial \eta}\,ds, \tag{7}$$

and equation (6) is rewritten as

$$\iint_{S_{i,j,k}} \sigma(x,y,z) \frac{\partial \phi(x,y,z)}{\partial \eta} \cdot$$
$$\cdot\, ds_{i,j,k} = -I(x_s, y_s, z_s), \tag{8}$$

where η is the outward normal and $S_{i,j,k}$ is the surface enclosing the elemental volume $\Delta V_{i,j,k}$. It is seen from equation (7) that over every element of R and on the boundary Γ, the boundary conditions given by equation (5) can be directly implemented in the left-hand side of equation (8).

The surface integral in equation (8) along the bounding surface $S_{i,j,k}$ is subdivided into six sub-surfaces as indicated in Figure 2. For an interior node in the discretization grid, by approximating $\partial \phi / \partial \eta$ by central difference and integrating along each of the bounding faces of the elemental volume $\Delta V_{i,j,k}$, we get

$$\iint_{S_{i,j,k}} \sigma_{i,j,k} \cdot \frac{\partial \phi_{i,j,k}}{\partial \eta}\,ds_{i,j,k}$$
$$= \frac{\phi_{i,j-1,k} - \phi_{i,j,k}}{\Delta y_{j-1}} \left[\sigma_{i-1,j-1,k-1} \frac{\Delta z_{k-1}\Delta x_{i-1}}{4} \right.$$
$$\left. + \sigma_{i,j-1,k-1} \frac{\Delta z_{k-1}\Delta x_i}{4} + \sigma_{i-1,j-1,k} \cdot \right.$$
$$\left. \cdot \frac{\Delta x_{i-1}\Delta z_k}{4} + \sigma_{i,j-1,k} \frac{\Delta x_i\Delta z_k}{4} \right]$$
$$+ \frac{\phi_{i,j+1,k} - \phi_{i,j,k}}{\Delta y_j} \left[\sigma_{i-1,j,k-1} \frac{\Delta z_{k-1}\cdot\Delta x_{i-1}}{4} \right.$$
$$\left. + \sigma_{i,j,k-1} \frac{\Delta z_{k-1}\cdot\Delta x_i}{4} + \sigma_{i-1,j,k} \frac{\Delta x_{i-1}\cdot\Delta z_k}{4} \right.$$
$$\left. + \sigma_{i,j,k} \frac{\Delta x_i\Delta z_k}{4} \right]$$
$$+ \frac{\phi_{i+1,j,k} - \phi_{i,j,k}}{\Delta x_i} \left[\sigma_{i,j-1,k-1} \frac{\Delta y_{j-1}\cdot\Delta z_{k-1}}{4} \right.$$

$$\left. + \sigma_{i,j,k-1} \frac{\Delta y_j\cdot\Delta z_{k-1}}{4} + \sigma_{i,j-1,k} \frac{\Delta y_{j-1}\cdot\Delta z_k}{4} \right.$$
$$\left. + \sigma_{i,j,k} \frac{\Delta y_j\Delta z_k}{4} \right]$$
$$+ \frac{\phi_{i-1,j,k} - \phi_{i,j,k}}{\Delta x_{i-1}} \left[\sigma_{i-1,j-1,k-1} \frac{\Delta y_{j-1}\cdot\Delta z_{k-1}}{4} \right.$$
$$\left. + \sigma_{i-1,j,k-1} \frac{\Delta y_j\Delta z_{k-1}}{4} + \sigma_{i-1,j-1,k} \cdot \right.$$
$$\left. \cdot \frac{\Delta y_{j-1}\Delta z_k}{4} + \sigma_{i-1,j,k} \frac{\Delta y_j\Delta z_k}{4} \right]$$
$$+ \frac{\phi_{i,j,k-1} - \phi_{i,j,k}}{\Delta z_{k-1}} \left[\sigma_{i-1,j,k-1} \frac{\Delta x_{i-1}\Delta y_j}{4} \right.$$
$$\left. + \sigma_{i,j,k-1} \frac{\Delta x_i\Delta y_j}{4} + \sigma_{i-1,j-1,k-1} \frac{\Delta x_{i-1}\cdot\Delta y_{j-1}}{4} \right.$$
$$\left. + \sigma_{i,j-1,k-1} \frac{\Delta x_i\Delta y_{j-1}}{4} \right]$$
$$+ \frac{\phi_{i,j,k+1} - \phi_{i,j,k}}{\Delta z_k} \left[\sigma_{i-1,j,k} \frac{\Delta x_{i-1}\cdot\Delta y_j}{4} \right.$$
$$\left. + \sigma_{i,j,k} \frac{\Delta x_i\Delta y_j}{4} + \sigma_{i-1,j-1,k} \frac{\Delta x_{i-1}\Delta y_{j-1}}{4} \right.$$
$$\left. + \sigma_{i,j-1,k} \frac{\Delta x_i\Delta y_{j-1}}{4} \right]. \tag{9}$$

Substituting equation (9) in (8), we obtain, for an interior node (i,j,k), the discretized equation

$$\overset{ijk}{\underset{top}{C}} \cdot \phi_{i,j,k-1} + \overset{ijk}{\underset{bottom}{C}} \cdot \phi_{i,j,k+1} + \overset{ijk}{\underset{left}{C}} \cdot \phi_{i-1,j,k}$$
$$+ \overset{ijk}{\underset{right}{C}} \cdot \phi_{i+1,j,k} + \overset{ijk}{\underset{front}{C}} \cdot \phi_{i,j-1,k} + \overset{ijk}{\underset{back}{C}}$$
$$\cdot \phi_{i,j+1,k} + \overset{ijk}{\underset{P}{C}} \cdot \phi_{i,j,k} = I\,\delta(x_i - x_s) \cdot$$
$$\cdot \delta(y_j - y_s)\,\delta(z_k - z_s), \tag{10}$$

where $\overset{ijk}{\underset{top}{C}}$, the coupling coefficient between the nodes (i,j,k) and $(i,j,k-1)$, is

$$\frac{-1}{\Delta z_{k-1}} \left[\sigma_{i-1,j,k-1} \frac{\Delta x_{i-1}\Delta y_j}{4} + \sigma_{i,j,k-1} \cdot \right.$$
$$\left. \cdot \frac{\Delta x_i\Delta y_j}{4} + \sigma_{i-1,j-1,k-1} \frac{\Delta x_{i-1}\Delta y_{j-1}}{4} \right.$$

$$+ \sigma_{i,j-1,k-1} \frac{x_i y_{j-1}}{4} \Bigg]; \qquad (10a)$$

$\overset{ijk}{\underset{\text{bottom}}{C}}$, the coupling coefficient between the nodes (i, j, k) and $(i, j, k + 1)$, is

$$-\frac{1}{\Delta z_k} \Bigg[\sigma_{i-1,j,k} \frac{\Delta x_{i-1}\Delta y_j}{4} + \sigma_{i,j,k} \frac{\Delta x_i \Delta y_j}{4}$$

$$+ \sigma_{i-1,j-1,k} \frac{\Delta x_{i-1}\Delta y_{j-1}}{4} + \sigma_{i,j-1,k} \cdot$$

$$\cdot \frac{\Delta x_i \Delta y_{j-1}}{4} \Bigg]; \qquad (10b)$$

$\overset{ijk}{\underset{\text{left}}{C}}$, the coupling coefficient between the nodes (i, j, k) and $(i - 1, j, k)$, is

$$-\frac{1}{\Delta x_{i-1}} \Bigg[\sigma_{i-1,j-1,k-1} \frac{\Delta y_{j-1}\Delta z_{k-1}}{4}$$

$$+ \sigma_{i-1,j,k-1} \frac{\Delta y_j \Delta z_{k-1}}{4} + \sigma_{i-1,j-1,k} \cdot$$

$$\cdot \frac{\Delta y_{j-1}\Delta z_k}{4} + \sigma_{i-1,j,k} \frac{\Delta y_j \Delta z_k}{4} \Bigg]; \qquad (10c)$$

$\overset{ijk}{\underset{\text{right}}{C}}$, the coupling coefficient between the nodes (i, j, k) and $(i + 1, j, k)$, is

$$-\frac{1}{\Delta x_i} \Bigg[\sigma_{i,j-1,k-1} \frac{\Delta y_{j-1}\Delta z_{k-1}}{4} + \sigma_{i,j,k-1} \cdot$$

$$\cdot \frac{\Delta y_j \Delta z_{k-1}}{4} + \sigma_{i,j-1,k} \frac{\Delta y_{j-1}\Delta z_k}{4} + \sigma_{i,j,k} \cdot$$

$$\cdot \frac{\Delta y_j \Delta z_k}{4} \Bigg]; \qquad (10d)$$

$\overset{ijk}{\underset{\text{front}}{C}}$, the coupling coefficient between the nodes (i, j, k) and $(i, j - 1, k)$, is

$$-\frac{1}{\Delta y_{j-1}} \Bigg[\sigma_{i-1,j-1,k-1} \frac{\Delta x_{i-1}\Delta z_{k-1}}{4}$$

$$+ \sigma_{i,j-1,k-1} \frac{\Delta x_i \Delta z_{k-1}}{4} + \sigma_{i-1,j-1,k} \cdot$$

$$\cdot \frac{\Delta x_{i-1}\Delta z_k}{4} + \sigma_{i,j-1,k} \frac{\Delta x_i \Delta z_k}{4} \Bigg]; \qquad (10e)$$

$\overset{ijk}{\underset{\text{back}}{C}}$, the coupling coefficient between the nodes (i, j, k) and $(i, j + 1, k)$, is

$$\frac{-1}{\Delta y_j} \Bigg[\sigma_{i-1,j,k-1} \frac{\Delta x_{i-1}\Delta z_{k-1}}{4} + \sigma_{i,j,k-1} \cdot$$

$$\cdot \frac{\Delta x_i \Delta z_{k-1}}{4} + \sigma_{i-1,j,k} \frac{\Delta x_{i-1}\Delta z_k}{4}$$

$$+ \sigma_{i,j,k} \cdot \frac{\Delta x_i \Delta z_k}{4} \Bigg]; \qquad (10f)$$

$\overset{ijk}{\underset{p}{C}}$, the self-coupling coefficient at node (i, j, k), is

$$-\Bigg[\overset{ijk}{\underset{\text{top}}{C}} + \overset{ijk}{\underset{\text{bottom}}{C}} + \overset{ijk}{\underset{\text{left}}{C}} + \overset{ijk}{\underset{\text{right}}{C}} + \overset{ijk}{\underset{\text{front}}{C}} + \overset{ijk}{\underset{\text{back}}{C}} \Bigg]. \quad (10g)$$

The self-adjoint difference equation (10) indicates that the solution ϕ at the (i, j, k) node is dependent only on the values of ϕ at the adjacent nodes $(i, j, k - 1)$, $(i, j, k + 1)$, $(i - 1, j, k)$, $(i + 1, j, k)$, $(i, j - 1, k)$, and $(i, j + 1, k)$. The node coupling coefficients are known functions of the geometry and predefined physical property distribution at all nodes in the set R.

The difference equations for the nodes located on the infinitely distant edge Γ of the set R are somewhat altered from that of an interior node, since the asymptotic mixed-boundary condition is to be implemented at these node locations. At all nodes on the ground surface $(z = 0)$, the Neumann condition is implemented as $\sigma(\partial \phi / \partial z) = 0$. For all other nodes located on the remaining faces, edges, and corners, the mixed boundary condition $\sigma(\partial \phi / \partial \eta) = -(\alpha \phi / r) \cos \theta$ [from equation (5)] is directly implemented while integrating over the appropriate bounding surfaces, for the outward normal η oriented, in the x-, y-, or z-directions. For brevity, the modified difference equations for only two typical locations of nodes on Γ are illustrated in the following.

Coupling coefficients for the difference equation (10) modified for a node (i, j, k) located on the bottom face (*excluding the edges and corner locations on this plane*) of the grid is given as

$$\overset{ijk}{\underset{\text{top}}{C}} = -\frac{1}{\Delta z_{k-1}} \Bigg[\sigma_{i-1,j,k-1} \frac{\Delta x_{i-1}\Delta y_j}{4}$$

$$+ \sigma_{i,j,k-1} \frac{\Delta x_i \Delta y_j}{4} + \sigma_{i-1,j-1,k-1} \cdot$$

$$\cdot \frac{\Delta x_{i-1}\Delta y_{j-1}}{4} + \sigma_{i,j-1,k-1} \frac{\Delta x_{i-1}\Delta y_{j-1}}{4} \Bigg];$$

$$\overset{ijk}{\underset{\text{bottom}}{C}} = 0.0,$$

$$\overset{ijk}{\underset{\text{left}}{C}} = -\frac{1}{\Delta x_{i-1}} \Bigg[\sigma_{i-1,j-1,k-1} \frac{\Delta y_{j-1}\Delta z_{k-1}}{4}$$

$$+ \ \sigma_{i-1, j, k-1} \ \frac{\Delta y_j \Delta z_{k-1}}{4} \Bigg],$$

$$\overset{ijk}{\underset{\text{right}}{C}} = - \frac{1}{\Delta x_i} \Bigg[\sigma_{i, j-1, k-1} \ \frac{\Delta y_{j-1} \Delta z_{k-1}}{4}$$

$$+ \ \sigma_{i j, k-1} \ \frac{\Delta y_j \Delta z_{k-1}}{4} \Bigg],$$

$$\overset{ijk}{\underset{\text{front}}{C}} = - \frac{1}{\Delta y_{j-1}} \Bigg[\sigma_{i-1, j-1, k-1} \ \frac{\Delta x_{i-1} \Delta z_{k-1}}{4}$$

$$+ \ \sigma_{i, j-1, k-1} \ \frac{\Delta x_i \Delta z_{k-1}}{4} \Bigg],$$

$$\overset{ijk}{\underset{\text{back}}{C}} = - \frac{1}{\Delta y_j} \Bigg[\sigma_{i-1, j, k-1} \ \frac{\Delta x_{i-1} \Delta z_{k-1}}{4}$$

$$+ \ \sigma_{i, j, k-1} \ \frac{\Delta x_i \Delta z_{k-1}}{4} \Bigg],$$

and

$$\overset{ijk}{\underset{p}{C}} = - \Bigg[\overset{ijk}{\underset{\text{top}}{C}} + \overset{ijk}{\underset{\text{left}}{C}} + \overset{ijk}{\underset{\text{right}}{C}} + \overset{ijk}{\underset{\text{front}}{C}} + \overset{ijk}{\underset{\text{back}}{C}} \Bigg] - \overset{ijk}{\underset{\text{top}}{C}}$$

$$\cdot \ \frac{|z_s - z_k| \Delta z_{k-1}}{r},$$

where r is the radial distance from the source point to the node (i, j, k).

Similarly, the coupling coefficients for a node (i, j, k) located on Γ at the *top, back,* and *right* corner of the discretization grid are derived as

$$\overset{ijk}{\underset{\text{top}}{C}} = \overset{ijk}{\underset{\text{back}}{C}} = \overset{ijk}{\underset{\text{right}}{C}}$$

$$\overset{ijk}{\underset{\text{bottom}}{C}} = - \sigma_{i-1, j-1, k} \ \frac{\Delta x_{i-1} \Delta y_{j-1}}{4 \Delta z_k},$$

$$\overset{ijk}{\underset{\text{left}}{C}} = - \sigma_{i-1, j-1, k} \ \frac{\Delta y_{j-1} \Delta z_k}{4 \Delta x_{i-1}},$$

$$\overset{ijk}{\underset{\text{front}}{C}} = - \sigma_{i-1, j-1, k} \ \frac{\Delta x_{i-1} \Delta z_k}{4 \Delta y_{j-1}},$$

and

$$\overset{ijk}{\underset{p}{C}} = - \Bigg[\overset{ijk}{\underset{\text{bottom}}{C}} + \overset{ijk}{\underset{\text{left}}{C}} + \overset{ijk}{\underset{\text{front}}{C}} \Bigg]$$

$$- \Bigg[\frac{\overset{ijk}{\underset{\text{bottom}}{C}} |z_s - z_k| \cdot \Delta z_k + \overset{ijk}{\underset{\text{left}}{C}} \cdot |x_s - x_i| \cdot \Delta x_{i-1}}{r^2}$$

$$+ \ \frac{\overset{ijk}{\underset{\text{front}}{C}} |y_j - y_s| \cdot \Delta y_{j-1}}{r^2} \Bigg].$$

In applying the mixed-boundary condition at the nodes located on the edge Γ, the radial distance to all the relevant nodes may be evaluated from the central point on the top surface of the prismatic mesh. While for different source locations the corresponding radial distances are slightly different, in the asymptotic limit, at Γ, no substantial error arises from this assumption. This assumption also enables the coupling coefficients thus generated to be invariant for any arbitrary source location. It is found experimentally that this mixed-boundary condition at the edges of the grid produces a solution for ϕ that allows a considerably better fit to the analytically computed solution at large distances from the source location.

MATRIX FORMULATION

The self-adjoint difference equation (10) is obtained for each node in the set R, once the appropriate coupling coefficients are derived using the proper boundary conditions. The sets of difference equations for each node are then assembled into a global or capacitance matrix form. In the course of the assembly, each node is numbered in an order to minimize the bandwidth of the matrix (Zienkiewicz, 1971). The set of simultaneous equations for all the nodes in the grid can be written symbolically as

$$[C][\phi] = [S], \tag{11}$$

where C is an $LMN \times LMN$ matrix, called the capacitance matrix, and is a function only of the geometry and the physical property distribution in the grid. The vector ϕ consists of the unknown solutions of the total potential at all the nodes, and the vector S contains the source terms of charge injection. It is to be noted that for multiple source locations, the C-matrix remains unaltered and a single decomposition of this matrix provides solutions for multiple S vectors, through repeated back-substitutions.

The capacitance matrix C has the following properties: (1) $C_{pp} > 0, p = 1, 2, 3 \ldots, LMN$; (2) $C_{pp} \geq$

$$\sum_{\substack{q=1 \\ q \neq p}}^{LMN}$$

$|C_{p, q}|, p = 1, 2, \ldots, LMN$, i.e., C is diagonally dominant; (3) C is symmetric, sparse, and banded with only six nonzero codiagonals; (4) C is irreducible and has a strongly connected graph (Varga, 1962); and (5) C possesses Young's property A (Young, 1954).

It has been shown by Varga (1962) that the explicit difference equations that give rise to the matrix C with properties described above, are inherently stable for irregular grid spacings.
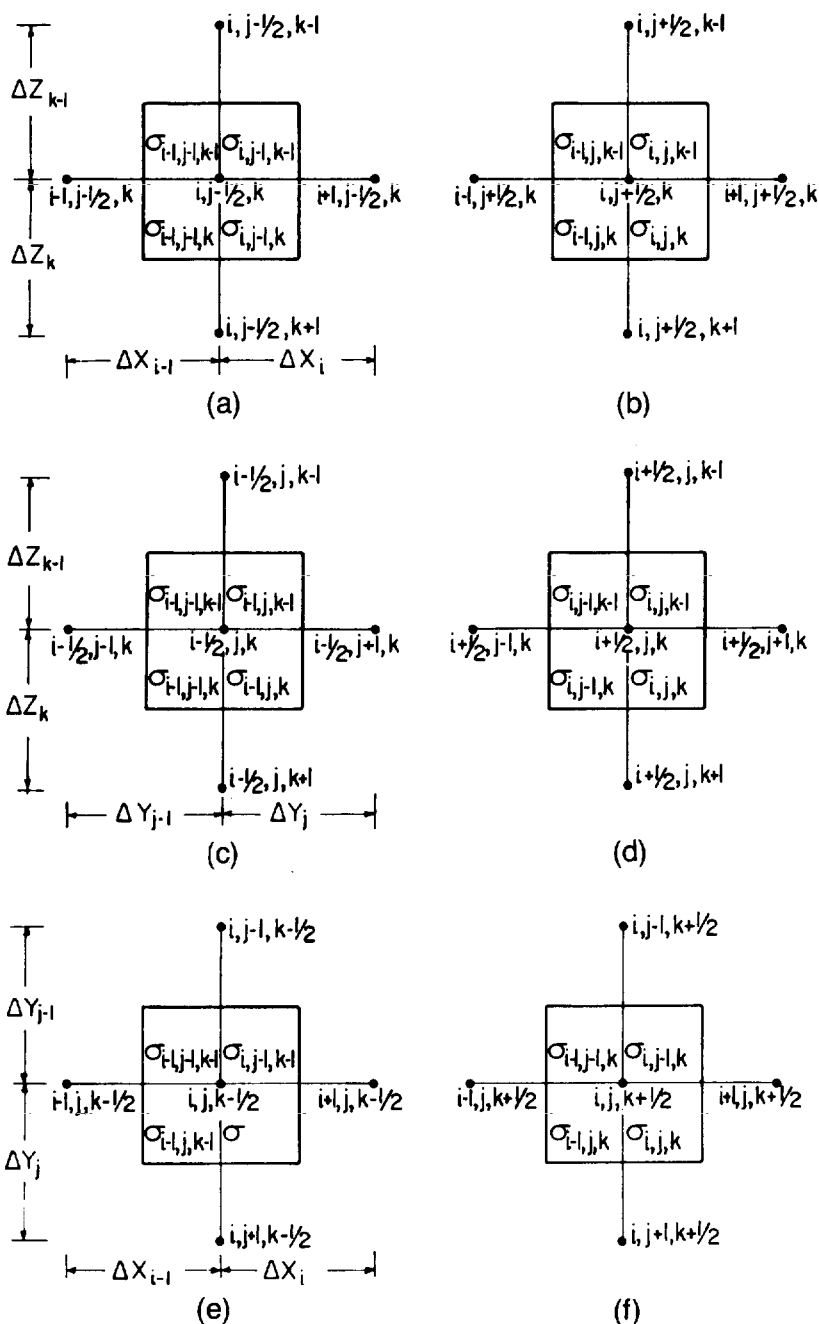
FIG. 2. Node locations and conductivity distribution on the six subsurfaces of $S_{i,j,k}$ about a node (i, j, k). (a) Front face (X-Z plane). (b) Back face (X-Z plane). (c) Left face (Y-Z plane). (d) Right face (Y-Z plane). (e) Top face (X-Y plane). (f) Bottom face (X-Y plane).

SOLUTION OF THE MATRIX EQUATION

In realistic simulations of the geologic models for electrical resistivity applications, the discretization grid generally results in 10,000 to 15,000 nodes at which the total potentials are to be evaluated for multiple current injection points. Such discretizations result in matrices that are rather unwieldy to handle even on a very large and fast computer (e.g., CDC 7600). We have attempted to solve such systems of equations using (1) successive over-relaxation methods, (2) incomplete Cholesky-conjugate gradient method, and (3) banded matrix decomposition techniques.

Equation (11) results in a very sparse banded matrix that has been solved traditionally using successive point overrelaxation (Southwell, 1946) or alternating direction iterative methods (e.g., Varga; 1962, Douglas and Rachford, 1956; Gunn, 1964). In these methods, an initial assumed distribution of ϕ_{ijk} over the grid is relaxed by successive refinements through iterations. The refinements in individual methods are either in terms of individual nodes, rows or columns of nodes, or of ϕ_{ijk} alternately along a column and a row. The refinement obtained upon an iteration is further updated by the use of an optimal overrelaxation factor or by successive use of the Chebychev overrelaxation acceleration parameter (Concus and Golub, 1973). In the large grids under consideration (approximately 10,000 to 15,000 nodal points), the successive overrelaxation and the alternating direction iterative techniques (Doss, 1977, private communication) require a minimum of 200–300 iteration sweeps through the entire grid for each location of the point source of current injection to produce solutions to an accuracy of 1–5 percent. In addition, the convergence rates of these iterative techniques are highly dependent on the dimensions of the grid spacings and the nature of the physical property distributions. Although the operation counts per iteration in these methods are relatively small (approximately 7 to 15 *LMN* multiplications at 0.3 to 1 sec of CPU time on the CDC 7600), the reliability of an acceptable convergence level, and reciprocity checks for arbitrary conductivity distributions, were often very poor.

A new iterative method called the incomplete Cholesky-conjugate gradient (ICCG) method for the solution of large, sparse systems of linear equations has been proposed by Meijerink and van der Vorst (1976). This method, when applied to the solution of large systems of elliptic partial differential equations, produced highly convergent solutions

10 to 100 times faster than the traditional successive overrelaxation or alternating direction iterative methods (Kershaw, 1977). The conjugate-gradient method as originally proposed by Hestenes and Stiefel (1952), when applied directly to solve for very large, sparse systems with a high condition number $(\lambda_{max} / \lambda_{min} = 10{-}100)$, is not very effective as an iterative method. However, in combination with an incomplete Cholesky decomposition of the **C** matrix, the iterative scheme is shown to be very efficient (Meijerink and van der Vorst, 1976).

In standard Cholesky decomposition, the symmetric, positive definite matrix **C** is written as

$$\mathbf{C} = \mathbf{LL}^T,$$

where **L** is lower triangular. With this decomposition of **C**, the equation $\mathbf{C}\phi = \mathbf{S}$ is easily solved as $\phi = (\mathbf{L}^T)^{-1}(\mathbf{L}^{-1}\mathbf{S})$. In practice, however, for a sparse matrix **C**, the **L**-matrix is full and is time-consuming to generate in its entirety. In the incomplete Cholesky-conjugate gradient method, an approximate decomposition of **C** is made such that

$$\mathbf{C} = \mathbf{LL}^T + E, \ (E = \text{error term}),$$

with the new factorized **L**-matrix having the same sparsity pattern imposed on it as the original **C**-matrix [ICCG (0), see Meijerink and van der Vorst, 1976]. With the new approximation of $(\mathbf{LL}^T)^{-1}$ for $\mathbf{C}^{-1}$, $\mathbf{L}^{-1}\mathbf{C}(\mathbf{L}^T)^{-1}$ will be an approximate identity matrix, and the conjugate-gradient method applied to the matrix $\mathbf{L}^{-1}\mathbf{C}(\mathbf{L}^T)^{-1}$ converges very rapidly. The solution of the system of equations $\mathbf{C}\phi = \mathbf{S}$ then is iteratively refined as indicated in the following algorithm (Kershaw, 1977):

$$r_0 = \mathbf{S} - \mathbf{C}\phi_0 \text{ and } p_0 = (\mathbf{LL}^T)^{-1}r_0,$$

ϕ_0 being any arbitrary assumed vector. Then

$$a_i = \frac{<r_i, (\mathbf{LL}^T)^{-1}r_i>}{<p_i, \mathbf{C}p_i>};$$

$$\phi_{i+1} = \phi_i + a_i p_i;$$

$$r_{i+1} = r_i - a_i \mathbf{C}p_i;$$

$$b_i = \frac{<r_{i+1}, (\mathbf{LL}^T)^{-1}r_{i+1}>}{<r_i, (\mathbf{LL}^T)^{-1}r_i>};$$

and

$$p_{i+1} = (\mathbf{LL}^T)^{-1}r_{i+1} + b_i p_i,$$

where the subscript i indicates the iteration cycle.
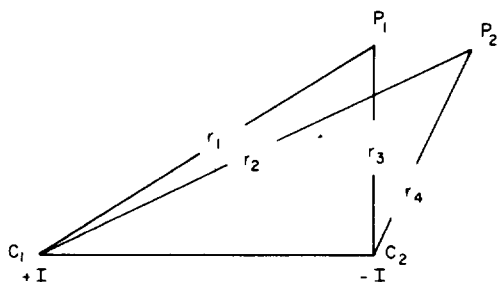
The efficiency of the method depends on the valid-

FIG. 3. Electrode locations in an arbitrary resistivity array.

ity of the approximation of $(\mathbf{L}\mathbf{L}^T)^{-1}$ for $\mathbf{C}^{-1}$. The self-adjoint equations of the difference form couple a node most strongly to its nearest adjacent nodes. Eliminating distant codiagonals in $\mathbf{L}$, thus neglecting coupling to more distant nodes, yields a good approximation. The operation count of such an iteration cycle is approximately 16 LMN multiplications (approximately 1 sec of CPU time on the CDC 7600 per iteration for a system of 12,000 equations). In the problem posed here, this method yields a solution with 1 to 3 percent accuracy for a large grid system (approximately 12,000 nodes) in about 30 to 40 iterations per source location. In our experiments, this method has given adequately accurate results and is recommended when the total potential solutions in the entire mesh need to be solved for only a few (1 to 5) current source locations.

The third method that has been used to solve the large, sparse system is based on a full-banded decomposition of the Cholesky type. The symmetric triangular decomposition of the banded $\mathbf{C}$-matrix is done in blocks using highly efficient, random disk access facilities and auxiliary out-of-core storage devices (Reid, 1972; Wilson et al, 1974). For a symmetric matrix system of 11,628 equations and a half-bandwidth of 205, the decomposition process requires about 230 sec of CPU time on the CDC 7600, and the back-substitution for each of the multiple source vectors requires approximately 7 sec of CPU time. In our experiments, this method has yielded the most accurate and stable solution, independent of the irregular mesh geometry or the physical property distributions. The economics of computation with this method to generate dipole-dipole or pole-dipole pseudo-sections (with 13 to 15 source vectors) is. competitive with that of the incomplete Cholesky-conjugate gradient method and is preferred because

of its inherent stability and high degree of accuracy.

The recent advances in solving very large and very sparse systems using minimal-degree ordering in conjunction with the nested dissection algorithms that take advantage of the nonzero element structure of the capacitance matrix (e.g., George and Liu, 1976; Reid, 1976; Sherman, 1975) will provide significantly more efficient solution techniques than the band or envelope methods previously used.

DETERMINATION OF THE APPARENT RESISTIVITY

In electrical resistivity surveys, a current source $+I$ and a current sink $-I$ are used to energize the conductive earth. A potential difference ΔV is measured between two points, P_1 and P_2, located at arbitrary azimuthal orientations (for surface arrays) or colatitudinal configurations (as in downhole-surface arrays). A parameter "apparent resistivity" is defined as a function

$$\rho_a = G \frac{\Delta V}{I},$$

where for the configuration illustrated in Figure 3,

$$G = 2\pi \frac{1}{(1/r_1 - 1/r_2 - 1/r_3 + 1/r_4)}.$$

For a homogeneous half-space, ρ_a is the true intrinsic resistivity of the medium. If, however, the lower semiinfinite medium has an inhomogeneous 3-D conductivity distribution, ρ_a indicates the resistivity of an apparent homogeneous half-space that results in an identical ΔV for the transmitter-receiver locations under consideration. All interpretations of electrical resistivity work are done using the apparent resistivity concept described above. It can be seen that the dc potential distribution at any point is the superposition of the solutions of two point sources of current located at the transmitting electrodes of amplitude $+I$ and $-I$ (the transmitting dipole).

MODEL COMPUTATIONS

In most of the results presented, a rectangular prismatic grid with $57 \times 17 \times 12$ (11,628) nodes was used. In the central, shallow part of the mesh, the nodes were finely spaced to provide a maximum resolution of one-quarter of the dipole length (used as an arbitrary unit distance) in the x-, y-, or z-direction for the model dimensions. To estimate the accuracy of the technique described in the previous sections, a two-layered earth model was simulated.

The resistivity of the top layer of unit thickness a was assumed to be 100 Ω-m and that of the bottom layer to be 10 Ω-m. A collinear dipole-dipole array was deployed with unit dipole length and with dipole separations $N = 1, 2, 3, \ldots, 10$. The numerical results are shown in Figure 4 by circles and the analytically computed response for the model by a solid line. The numerical results approach the analytic solution with an absolute accuracy of better than 5 percent. Further tests (not shown) made with analytical solutions for an outcropping contact, buried conductive sphere, and with numerical solutions for block-shaped buried 3-D inhomogeneities (Meyer, 1977; Bakbak, 1977) generally indicated good agreement, with an absolute accuracy in the range of 3 to 10 percent.

MODEL RESULTS

Dipole-dipole configuration

A series of models has been used in the following analysis to illustrate the effects of strike-length, depths of burial, conductivity contrast, and a conductive overburden layer for a single conductive inhomogeneity located in a dissipative half-space. A standard test model was chosen with dimensions $1 \times 2 \times 2$ in the x-, y-, and z-directions, respectively.

The surrounding host rock is assumed to have a resistivity of 100 Ω-m and the inhomogeneity is assigned a resistivity of 3 Ω-m.

Effect of the strike-length.—

(a) **Without a conductive overburden layer**—The apparent resistivity pseudo-sections along a profile line on the surface-oriented normal to the strike of the inhomogeneity are shown in Figures 5a, 5b, 5c, 5d, and 5e for strike-lengths of 1, 2, 4, 6, and 10 units, respectively. The profile line bisects the strike-length in each case. The pseudo-section for the same inhomogeneity with infinite strike-length is shown in Figure 5f. For strike-lengths up to about 6 units, the most remarkable feature is the appearance of a relative apparent resistivity high directly below the location of the inhomogeneity. The values for strike-lengths of 1, 2, and 4 are slightly larger than the resistivity of the surrounding medium, and this zone underlies a zone of low apparent resistivities observed at smaller dipole separations. This feature has also been observed by Dieter et al (1969) and Bakbak (1977). As the strike-length is increased, the flanking high zones grow in amplitude, while the high directly below the location of the inhomogeneity decreases in amplitude. The
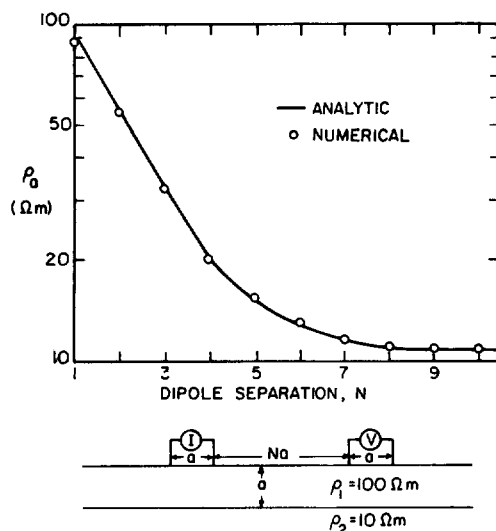

FIG. 4. Comparison of the analytic and numerical solution with finite-difference discretization over a two-layered earth model.

zone of low apparent resistivities is best described by noting the progression of the 80 Ω-m contour in Figures 5a–5f as the strike-length is increased. The low resistivity zone increases in size and the values decrease from approximately 20 percent below the half-space value to over 50 percent in the case of the infinite strike-length. With the strike-length of about 10 units, the pseudo-section closely resembles that of a 2-D inhomogeneity in both pattern and amplitude.

(b) **With a conductive overburden layer**— The effect of varying strike-lengths of the standardized inhomogeneity when it is overlain by a conductive overburden of thickness 0.5 units and resistivity 10 Ω-m illustrated in Figures 6a, 6b, and 6c for strike-lengths of 2 units, 6 units, and infinity, respectively. The conductive overburden substantially decreases the amplitude of the resistivity low. The horizontal spreading of the current lines due to the screening effect of the conductive overburden causes the 3-D model values to approach the 2-D values for a strike-length of only 6 units. At large dipole separations, $N = 7$ to 10, for a strike-length of 2 units (Figure 6a), the apparent resistivity values are somewhat higher than those for the 2-D model (Figure 6c).

MODEL 1 - 3D
DIPOLE - DIPOLE PSEUDO SECTION OF APPARENT RESISTIVITY
THE PROFILE LINE IS AT 90 DEGREES TO STRIKE AND IS AT Y=0.0

(a)

MODEL 2A - 3D

(b)

X-Z RESISTIVITY CROSS-SECTION OF THE MODEL AT Y=0
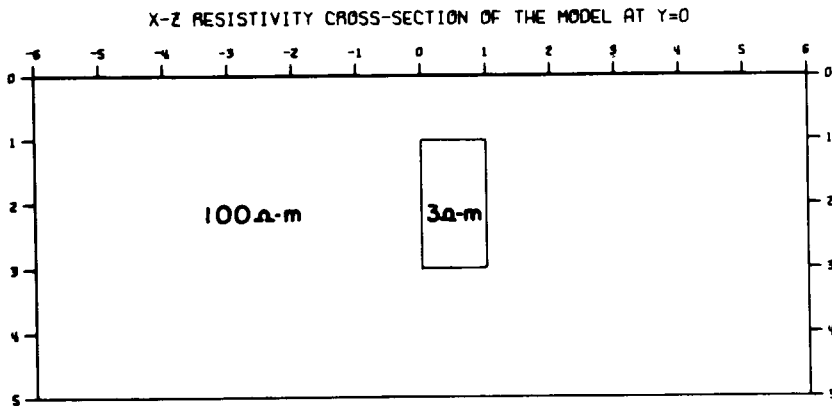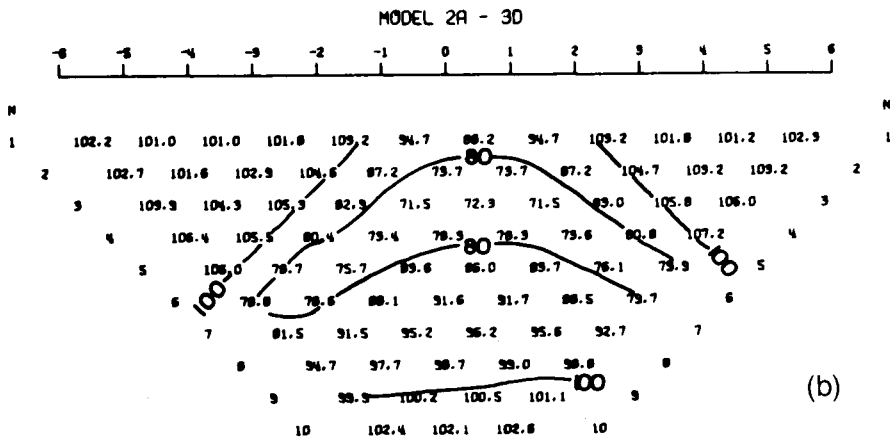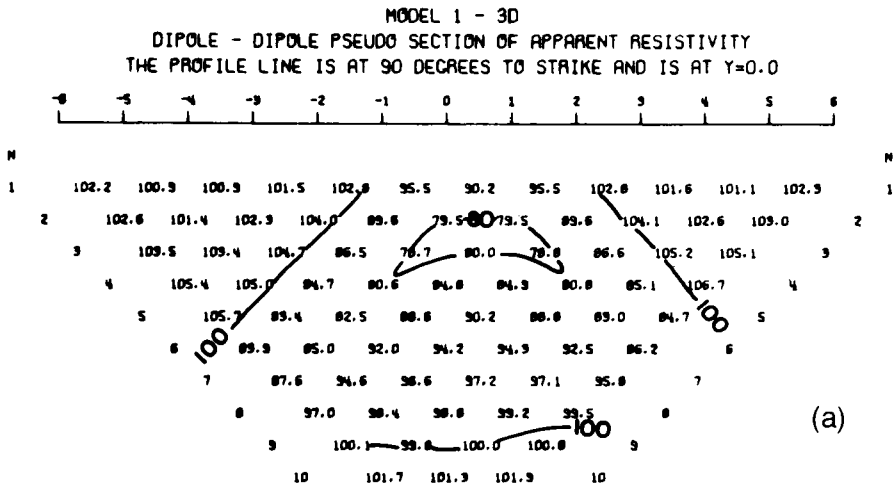
100 Ω-m   3 Ω-m

FIG. 5 a, b. Apparent resistivity pseudosections of the standard test model with strike-lengths of (a) 1.0 unit, (b) 2.0 units.

MODEL 3 - 3D
DIPOLE - DIPOLE PSEUDO SECTION OF APPARENT RESISTIVITY
THE PROFILE LINE IS AT 90 DEGREES TO STRIKE AND IS AT Y=0.0

(c)

MODEL 4 - 3D

(d)

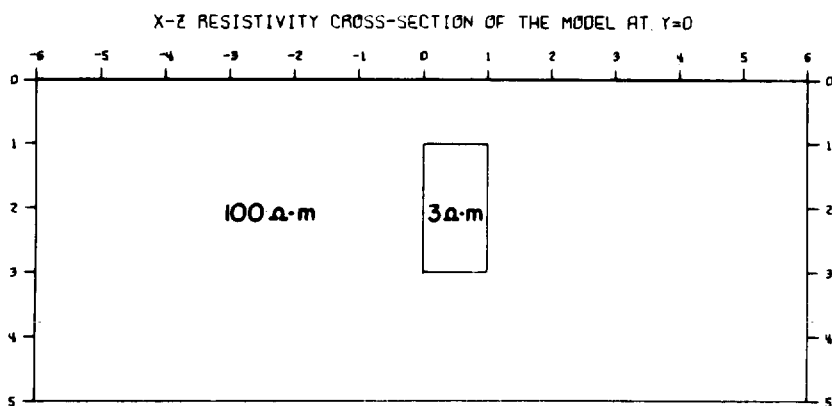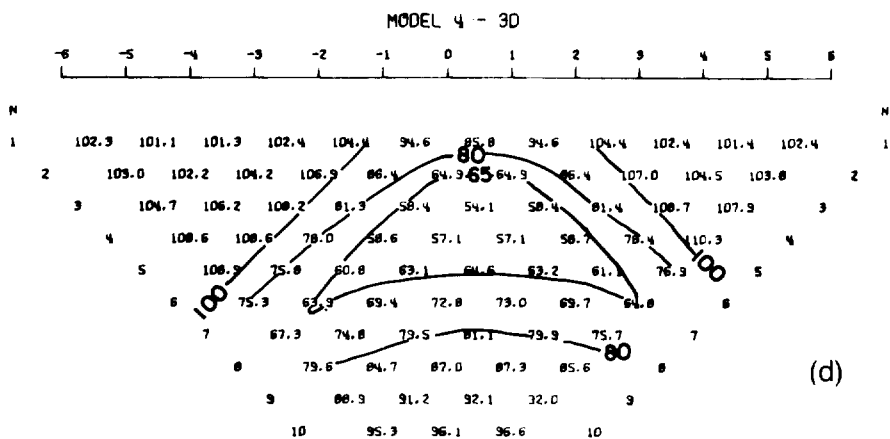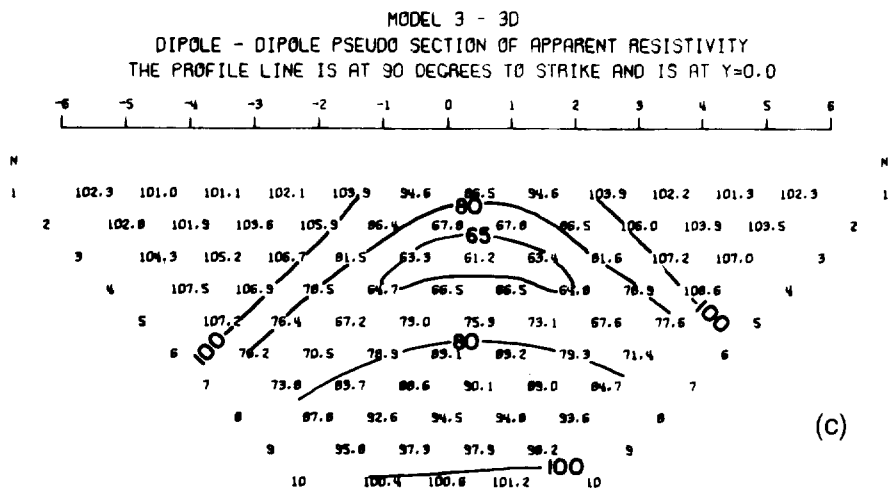X-Z RESISTIVITY CROSS-SECTION OF THE MODEL AT Y=0

FIG. 5 c, d. Apparent resistivity pseudosections of the standard test model with strike-lengths of (c) 4.0 units, (d) 6.0 units.

MODEL S - 30
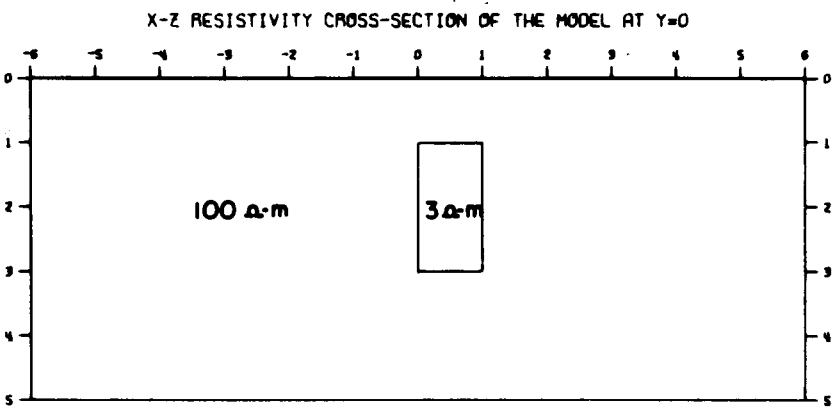DIPOLE - DIPOLE PSEUDO SECTION OF APPARENT RESISTIVITY
THE PROFILE LINE IS AT 30 DEGREES TO STRIKE AND IS AT Y=0.0

(e)

MODEL SH - 2D

(f)

X-Z RESISTIVITY CROSS-SECTION OF THE MODEL AT Y=0
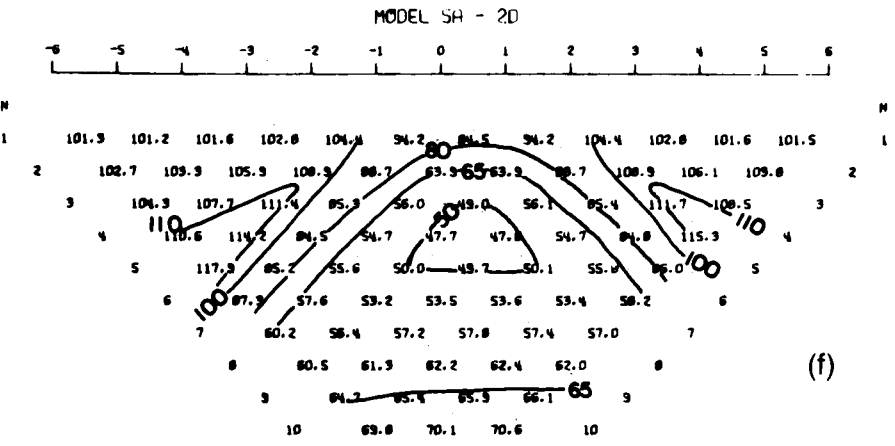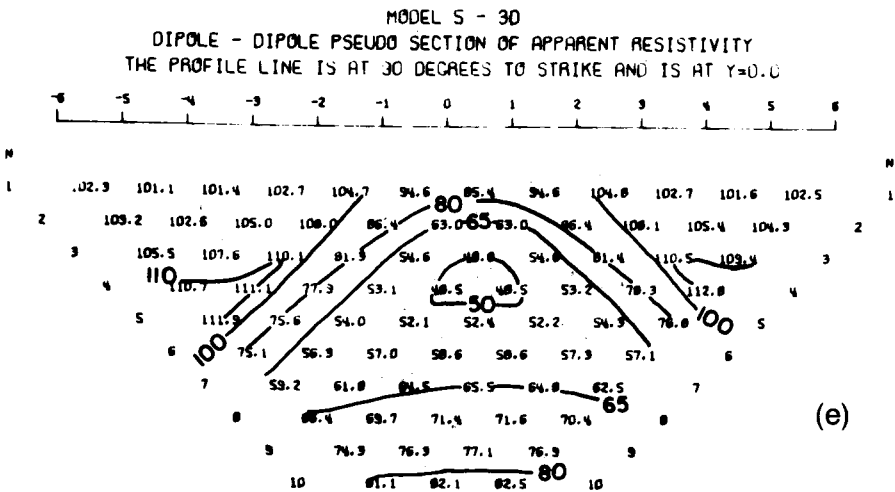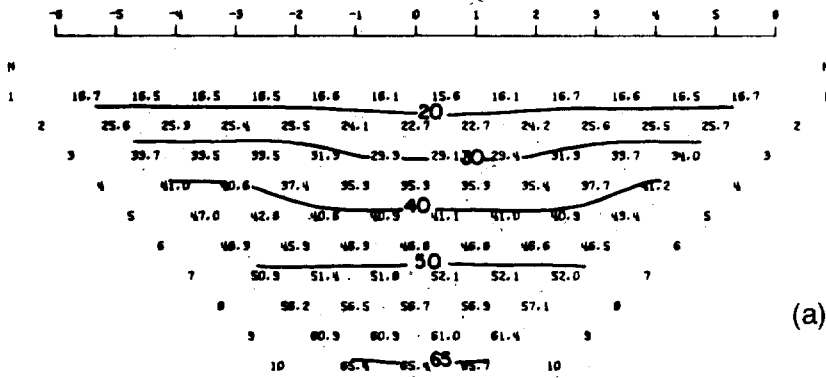

100 Ω·m   3 Ω·m

FIG. 5 e, f. Apparent resistivity pseudosections of the standard test model with strike-lengths of (e) 10.0 units, (f) infinity.

MODEL 6A - 3D
DIPOLE - DIPOLE PSEUDO SECTION OF APPARENT RESISTIVITY
THE PROFILE LINE IS AT 90 DEGREES TO STRIKE AND IS AT Y=0.0

(a)
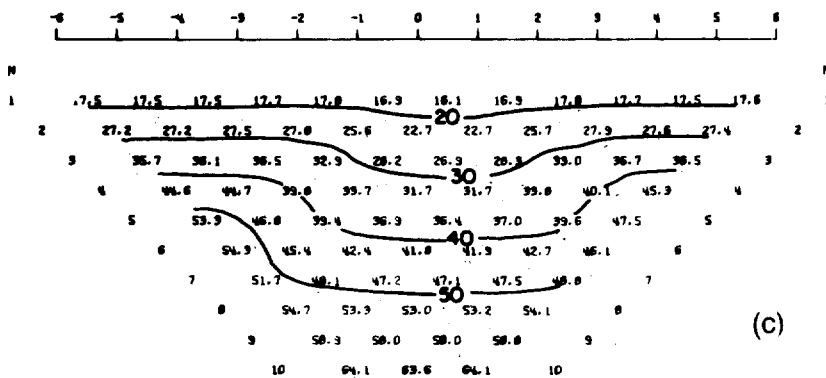
MODEL 7 -3D
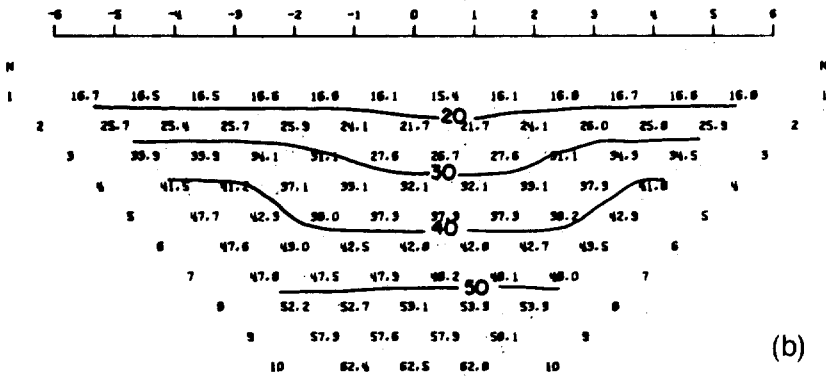
(b)

MODEL 8A - 2D

(c)

FIG. 6. Apparent resistivity pseudosections of the standard test model under a conductive overburden layer with strike-lengths of (a) 2.0 units, (b) 6.0 units, and (c) infinity.
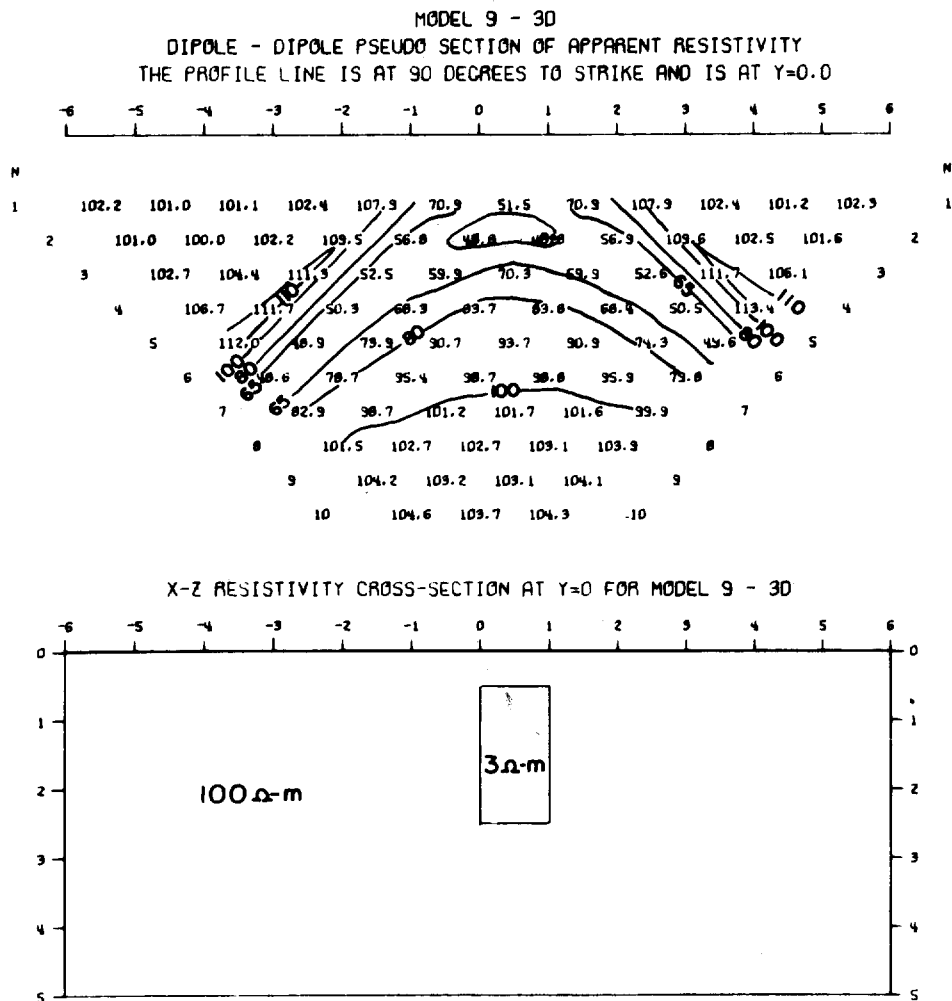
FIG. 7. Apparent resistivity pseudosections of the standard test model at a depth of burial of 0.5 units.

Unlike the case without overburden, the difference in the response pattern between the 3-D and 2-D models is much less. Were the low resistivity block of Figure 6c more deeply buried or less conductive, the anomaly would in all practical cases be indistinguishable from the 3-D block of Figure 6a, which has a strike-length of only 2 units.

Effect of depth of burial.—Figures 7 and 5b illustrate the apparent resistivity pseudo-sections for the standardized conductive inhomogeneity with strike-length of 2, at depths of 0.5 and 1.0 units, respectively. The low resistivity anomaly associated

with the body shows a sharp drop in amplitude with increasing depth of burial. The anomalous resistivity high observed directly below the body at large dipole separations grows in amplitude as the top of the inhomogeneity approaches the ground surface.

A conductive overburden layer of thickness 0.5 unit and resistivity 10 Ω-m overlies the standardized inhomogeneity with depths of burial of 0.5 unit and 1.0 unit in Figures 8 and 6a, respectively. The anomaly patterns are considerably more diagnostic for the shallower depth to the top of the body, although the anomaly amplitude is not very large. In our model studies, the response of such a conductive

MODEL 14 -3D
DIPOLE - DIPOLE PSEUDO SECTION OF APPARENT RESISTIVITY
THE PROFILE LINE IS AT 90 DEGREES TO STRIKE AND IS AT Y=0.0

| -6 | -5 | -4 | -3 | -2 | -1 | 0 | 1 | 2 | 3 | 4 | 5 | 6 |

N   N

1   16.7   16.5   16.6   16.8   17.8   11.8   10.1   11.8   17.8   16.8   16.6   16.8   1

2   25.7   25.5   26.1   27.8   16.7   17.2 —15— 17.2   16.7   27.9   26.2   25.9   2
                                              —20—

3   34.0   34.6   36.7   21.9   24.6   26.9 —30— 24.6   21.4   37.0   35.1   3

4   42.3   44.5   25.4   31.1   34.5   34.5   31.2   25.5   45.1   4

5   51.5   26.9   36.8   40.8 —40— 40.9   37.0   29.9   5

6   32.5   42.9   46.6   47.5 —50— 47.6   46.9   42.8   6

7   47.6   52.0   52.8   53.0   53.0   52.6   7

8   57.0   57.5   57.7   57.8   58.1   8

9   62.0   61.8   61.9   62.3   9

10   66.3   66.1 —65— 66.5   10

X-Z RESISTIVITY CROSS-SECTION AT Y=0 FOR MODEL 14 - 3D

| -6 | -5 | -4 | -3 | -2 | -1 | 0 | 1 | 2 | 3 | 4 | 5 | 6 |

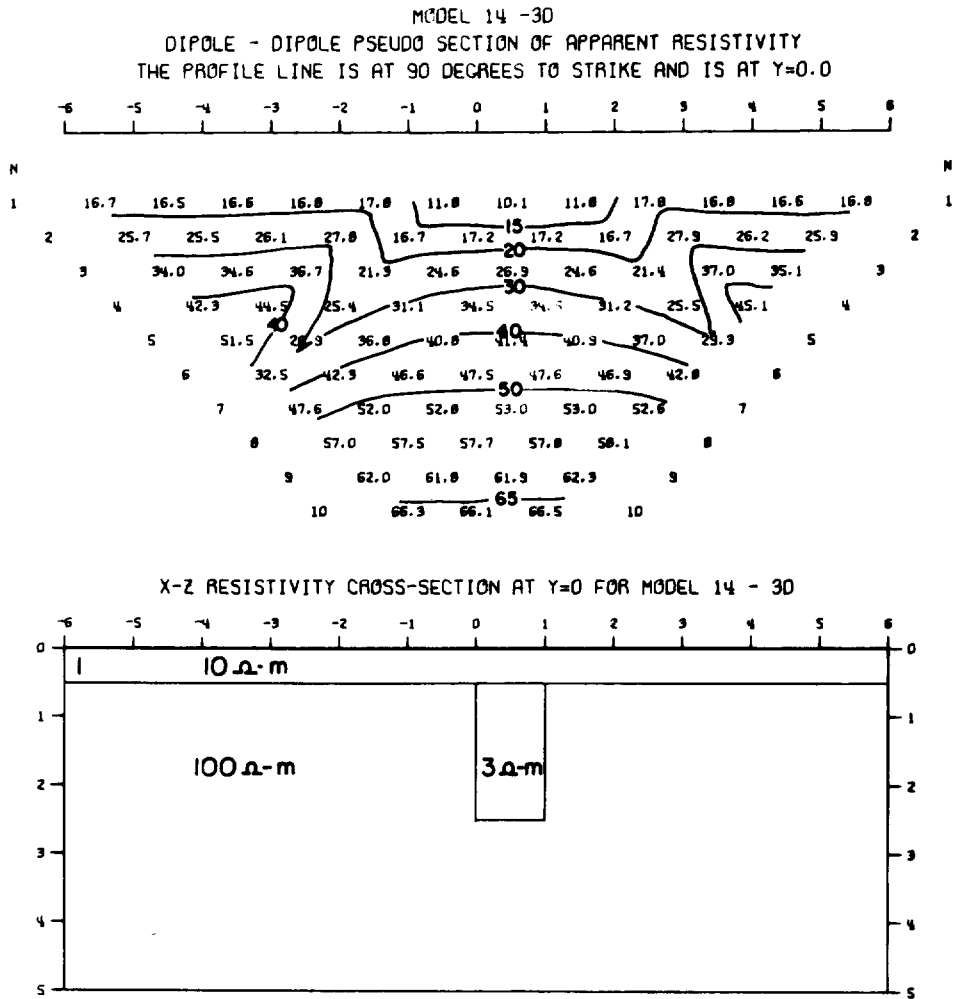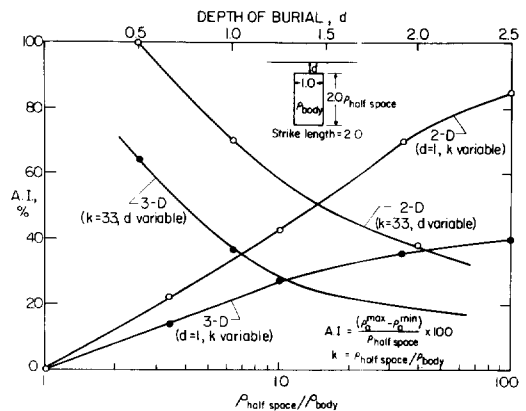1   10 Ω· m

100 Ω-m   3 Ω-m

FIG. 8. Apparent resistivity pseudosection of the standard test model located directly under a conductive overburden layer of thickness 0.5 units.

target appears to be indistinguishable from the two-layered earth response for depths of burial of the body greater than 1.5 units.

A summary of the effects of depth of burial and conductivity contrasts of the standardized 3-D body together with a 2-D model of identical cross-section is shown in Figure 9. A normalized anomaly index is defined as

$$A.I. = \frac{\rho_a^{max} - \rho_a^{min}}{\rho_{half-space}} \times 100 \text{ percent.}$$

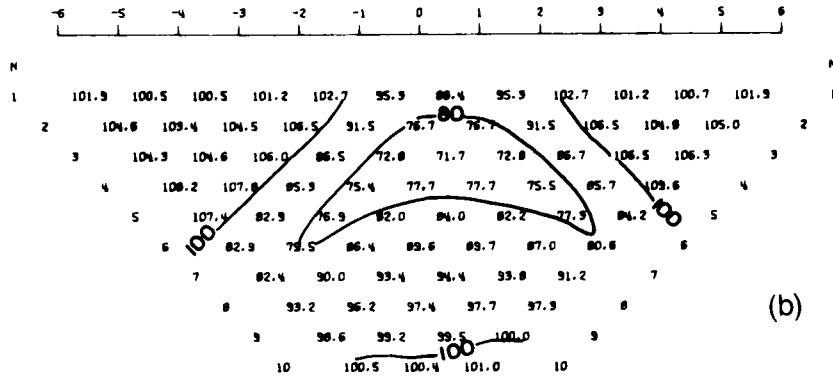FIG. 9. Characteristic diagram of the Anomaly Indices (A.I.) for the standard test model.

DEPTH OF BURIAL, d

2-D
(d=1, k variable)

2-D
(k=33, d variable)

3-D
(k=33, d variable)

3-D
(d=1, k variable)

$$AI = \frac{(\rho_a^{max} - \rho_a^{min})}{\rho_{half\ space}} \times 100$$

$$k = \rho_{half\ space} / \rho_{body}$$

$\rho_{half\ space} / \rho_{body}$

MODEL 2B - 3D, Y=+0.5
DIPOLE - DIPOLE PSEUDO SECTION OF APPARENT RESISTIVITY
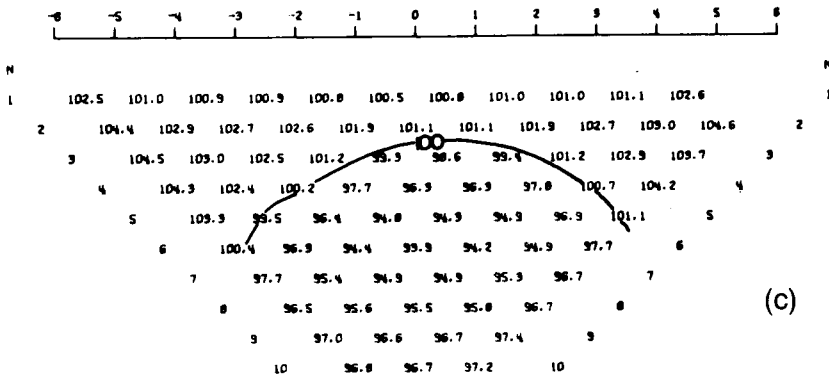THE PROFILE LINE IS AT 90 DEGREES TO STRIKE

(a)

MODEL 2C - 3D, Y=+1.0

(b)
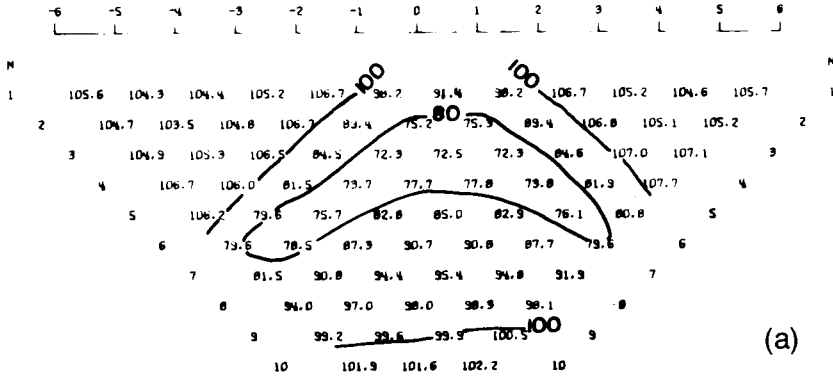
MODEL 2D - 3D, Y=+3.0

(c)

FIG. 10. Apparent resistivity pseudosections of the standardized inhomogeneity of strike-length 2.0 units with the profile line shifted from the center of the body by (a) 0.5 unit, (b) 1.0 unit and (c) 3.0 units in the strike direction.

In the pseudosections of apparent resistivity, there appear zones of relatively high as well as low values, due to the presence of a conductive target. The anomaly index (A.I.) is a measure of the distortion in the half-space response caused by the inhomogeneity. In the characteristic diagram, the A.I. measure shows substantially higher distortion for 2-D targets compared to the 3-D targets of identical cross-section for various conductivity contrasts. With increased depth of burial, the rate of decrease in the anomaly level for both 2-D and 3-D bodies is approximately the same, although for comparable depths of burial the 3-D targets have much lower detectability (A.I. values).

It is also interesting to note that the A.I. values of 3-D bodies show a saturation for conductivity contrasts in excess of about 30. The A.I. for the 2-D case is still rising for a contrast of 100.

Profile lines shifted along the strike direction.

The strike-extent of a 3-D inhomogeneity could be mapped by observations made along parallel profile lines normal to the strike. For the standardized inhomogeneity, with dimensions $1 \times 2 \times 2$ in the x-, y-, z-directions, respectively, this effect is shown in pseudosections illustrated in Figures 6a, 10a, 10b and 10c for line shifts of 0.0, 0.5, 1.0, and 3.0 units, respectively, from the center of the surface projection of the inhomogeneity. The patterns in the apparent resistivity pseudosections do not alter appreciably from $y = 0$ (line bisecting the strike-length) to $y = 0.5$. For the pseudosection at $y = 1.0$ unit (along the surface projection of one edge of the body), the resistivity low zone shrinks laterally, while the basic pattern is maintained. For the pseudo-section at $y = 3.0$ units (Fig. 10c), the effect of the inhomogeneity is substantially reduced in that a small anomaly of the order of 5 percent indicates the presence of a conductive target on one side of the profile. With only one pseudosection, say Figure 10c, it would be impossible to deduce whether a conductive inhomogeneity were buried directly beneath the line or off to one side.

Patterns very similar to these are observed when the standardized inhomogeneity is overlain by a conductive overburden layer.

A BASIN AND RANGE GEOTHERMAL MODEL

An analysis of a more complicated model has arisen from a field study of the geothermal potential in a typical basin and range geologic section. In such sections, the sediments are typically separated by
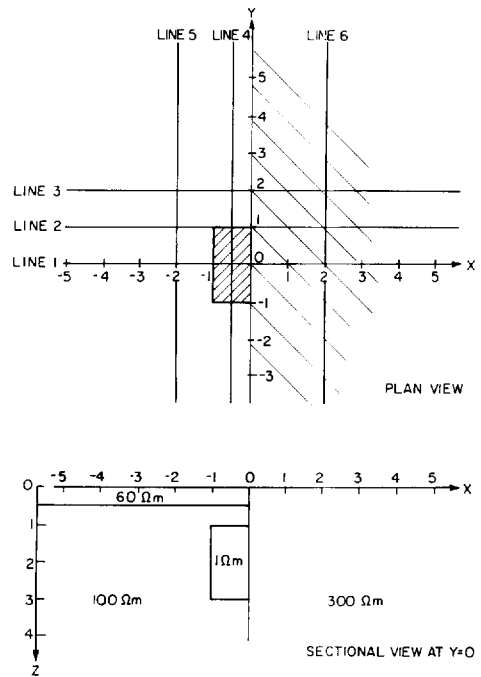

FIG. 11. Plan and sectional views of the basin and range geothermal model.

steep normal faults from more resistive bedrock of the adjacent ranges. The bounding faults are hypothesized to be conduits for ascending hot water. Portions of the sedimentary section adjacent to the fault could act as reservoirs for hot water. To date, modeling used in the interpretation of resistivity surveys has considered only reservoirs of infinite strike-length. It is probable, however, that only certain portions of the fault act as conduits so that the resulting reservoir would have limited strike-length.

To assess the effectiveness of the resistivity method in such cases, we have analyzed the responses of the 3-D model shown in Figure 11. Six profile lines oriented parallel and perpendicular to the strike are indicated in the plan view. The vertical sectional view on the line through the center of the body and perpendicular to strike also is shown. Pseudosections of apparent resistivities on these lines are shown in Figures 12a to 12f.

Two additional pseudo-sections along line 1 are shown for the fault model with no conductivity inhomogeneity (Figure 13) and with a conductive inhomogeneity of infinite strike-length (Figure 14). The most striking result is that for line 1 on a profile

MODEL FAULT 3D - LINE 1, Y=0.0
DIPOLE - DIPOLE PSEUDO SECTION OF APPARENT RESISTIVITY
THE PROFILE LINE IS AT 90 DEGREES TO STRIKE
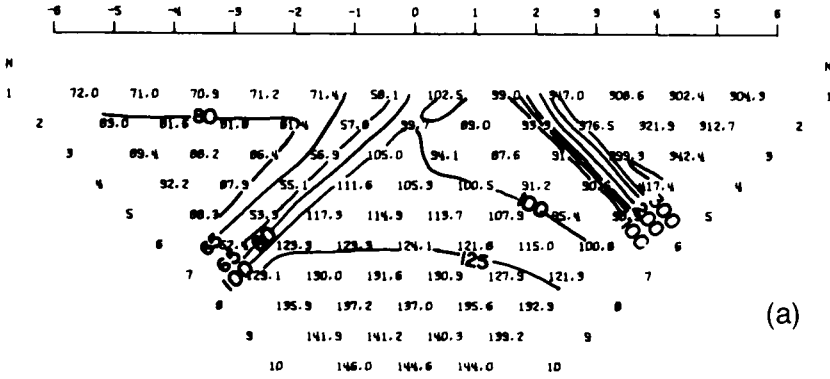
(a)

MODEL FAULT 3D - LINE 2, Y=+1.0
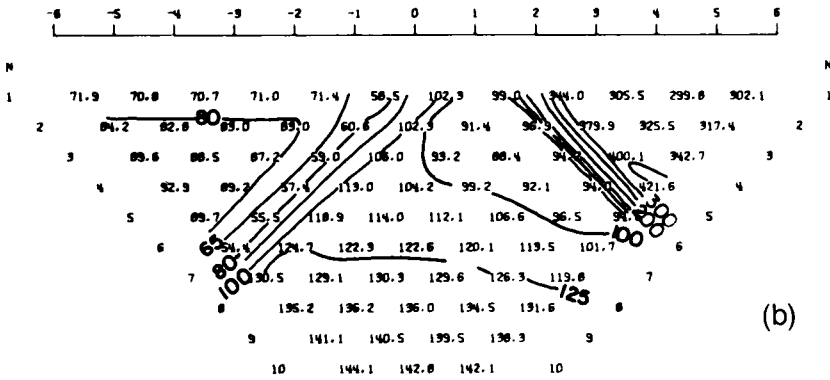
(b)

MODEL FAULT 3D - LINE 3, Y=+2.0

(c)

FIG. 12 a, b, c. Apparent resistivity pseudosections of the basin and range model along (a) profile line 1, (b) profile line 2, and (c) profile line 3.

MODEL FAULT 3D - LINE 4, X=-4.5
DIPOLE - DIPOLE PSEUDO SECTION OF APPARENT RESISTIVITY
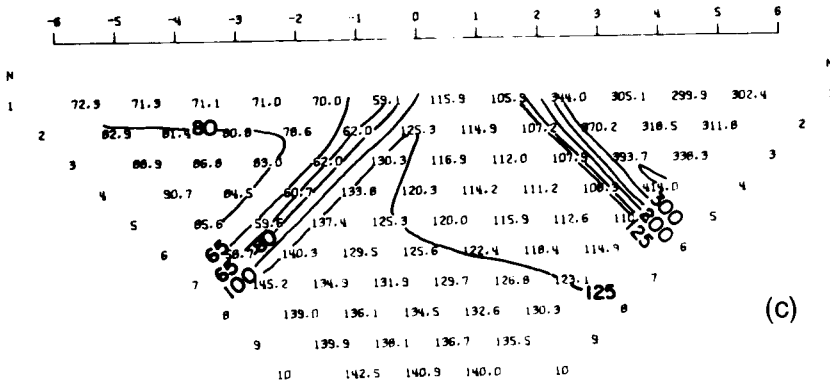THE PROFILE LINE IS AT 90 DEGREES TO STRIKE

(d)

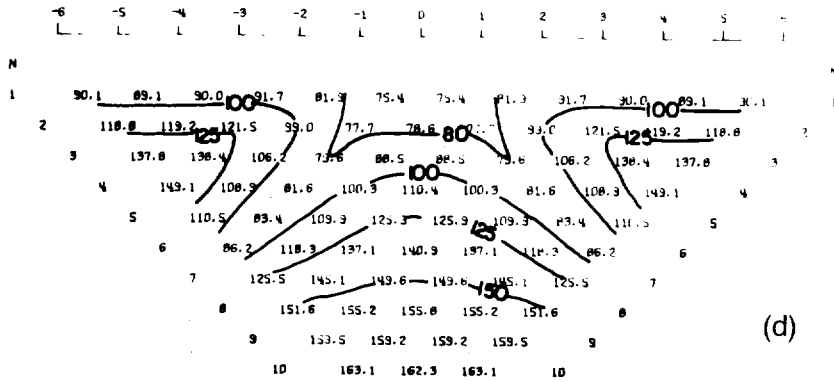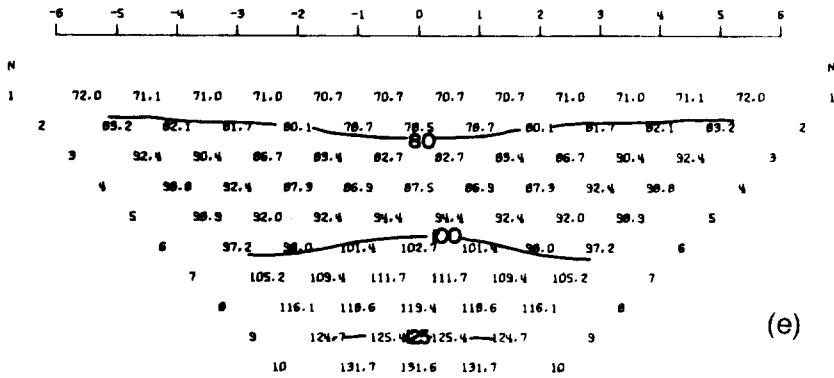MODEL FAULT 3D - LINE 5, Y=-2.0

(e)

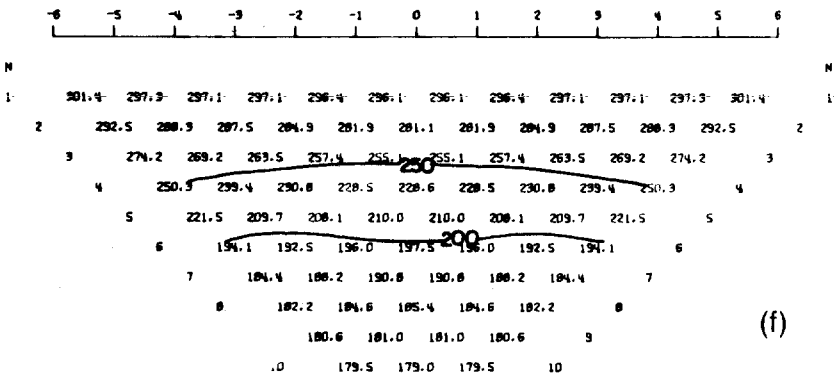MODEL FAULT 3D - LINE 6, X=+2.0

(f)

FIG. 12 d, e, f. Apparent resistivity pseudosections of the basin and range model along (d) profile line 4, (e) profile line 5, and (f) profile line 6.

MODEL FAULT A - 2D
DIPOLE - DIPOLE PSEUDO SECTION OF APPARENT RESISTIVITY
THE PROFILE LINE IS AT 90 DEGREES TO STRIKE AND IS AT Y=0.0

```
     -6    -5    -4    -3    -2    -1     0     1     2     3     4     5     6
     L_____L_____L_____L_____L_____L_____L_____L_____L_____L_____L_____L_____L

 N                                                                              N

  1    79.2   72.9   72.7   72.3   70.7   61.1   122.3  109.4  944.3  909.1  904.3  903.8    1

  2    84.6   89.7   80   82.5   73.1   93.6   140.7  129.5  113.4  971.3  918.9  910.0    2

  3    89.4   87.0   81.8   83.0   99.1   199.0  190.0  116.7  924.6  925.0    3

  4    90.4   89.4   82.3   154.5  144.3  198.1  190.6  915.4  997.0    4

     S    85.0   82.0   156.5  149.1  149.3  198.2  191.8  117.0    S

      6            162.7  153.1  147.7  149.6  199.6  194.4    6

       7    167.1  156.4  150.3  147.2  144.9  141.7    7

        8    162.0  155.6  151.8  149.3  147.8    8

         9    158.5  153.9  151.3  150.9    9

          10    159.0  155.5  154.4    10
```

X-Z RESISTIVITY CROSS-SECTION AT Y=0 FOR FAULT A -2D

```
     -6    -5    -4    -3    -2    -1     0     1     2     3     4     5     6
   0 L_____L_____L_____L_____L_____L_____L_____L_____L_____L_____L_____L_____L 0
     |                                      |                                |
     |            60 Ω·m                    |                                |
   1 |                                      |                                | 1
     |                                      |                                |
     |                                      |                                |
   2 |                                      |                                | 2
     |          100 Ω·m                     |          300 Ω·m               |
   3 |                                      |                                | 3
     |                                      |                                |
   4 |                                      |                                | 4
     |                                      |                                |
   5 |_____|_____| 5
```
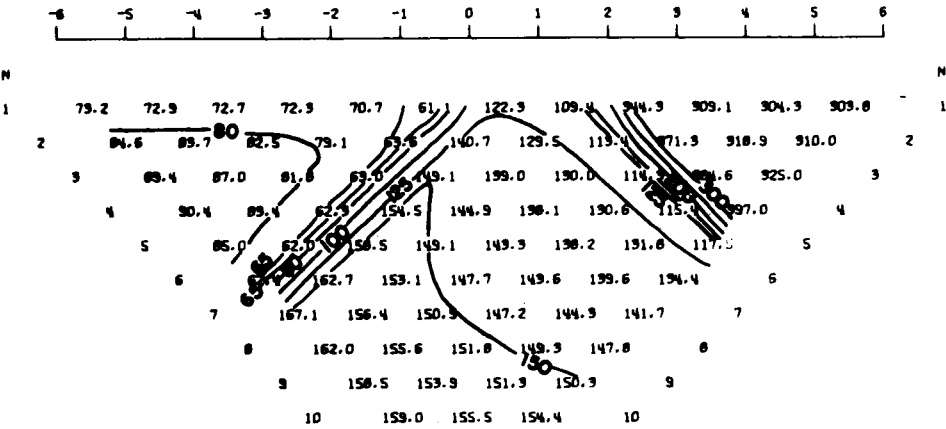
FIG. 13. Apparent resistivity pseudosection of the 2-D basin and range model with no conductive reservoir zone near the fault.

perpendicular to strike, the anomaly caused by the 3-D inhomogeneity (Figure 12a) is considerably less than its 2-D counterpart (Figure 14). The 2-D conductive reservoir (Figure 14) could be delineated easily, but the pseudosection of Figure 12a could be interpreted as being caused by a sloping fault contact displaced somewhat to the left of its actual position. The anomaly patterns in the pseudosection of lines 1, 2, and 3 (Figures 12a, b, and c), and in the pseudosection of Figure 13, are very similar. Each could be interpreted as a fault contact with only subtle differences in location and dip.

For profile line 4 (Figure 12d), parallel to strike and directly over the body, the anomaly is quite distinctive and clearly defines the location and extent of the conductor. Parallel lines not over the body (Figures 12e and 12f) show typical responses of quarter-space models and do not show any effect of the nearby body. While these lines can be used to delineate the width of the body, they also reveal the importance of closely spaced lines in detecting the body.

Reservoirs of significant dimension could easily be missed using the conventional approach of orient-

MODEL FAULT B - 2D
DIPOLE - DIPOLE PSEUDO SECTION OF APPARENT RESISTIVITY
THE PROFILE LINE IS AT 90 DEGREES TO STRIKE AND IS AT Y=0.0

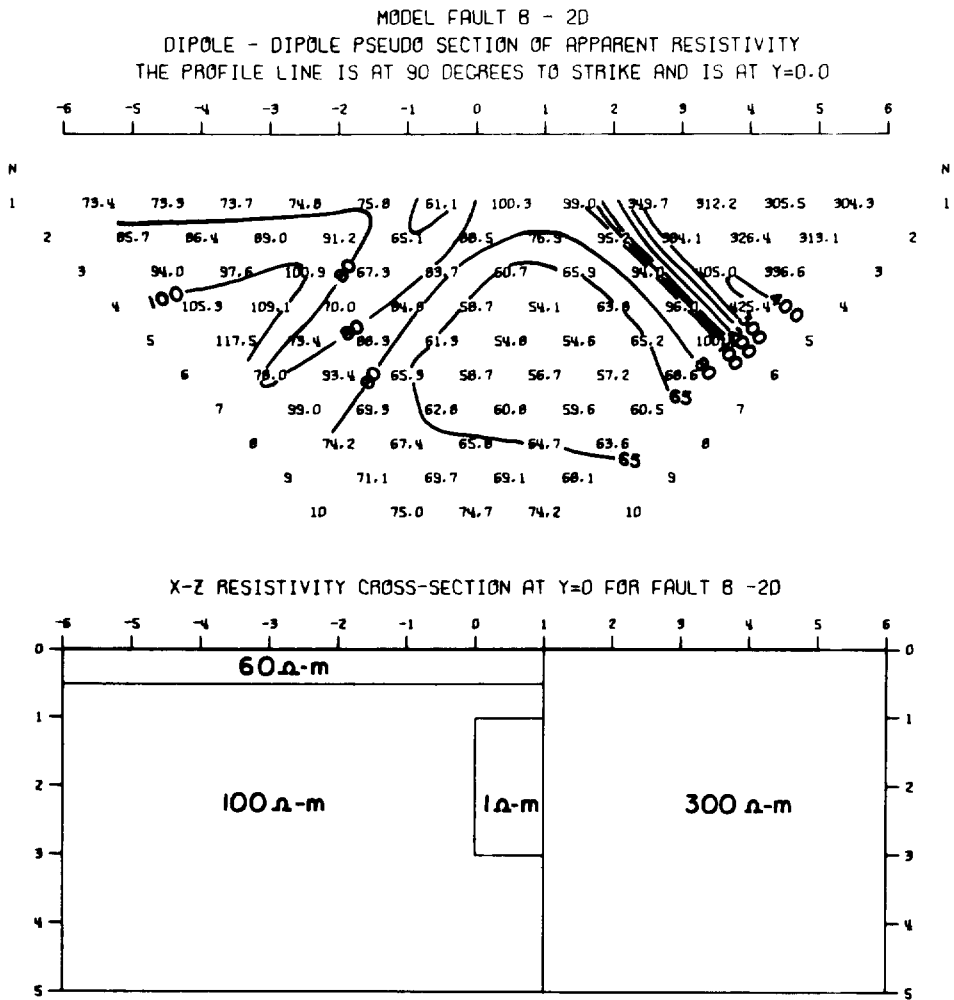X-Z RESISTIVITY CROSS-SECTION AT Y=0 FOR FAULT B -2D

FIG. 14. Apparent resistivity pseudosection of the 2-D basin and range model with the conductive reservoir zone of infinite strike-length.

ing dipole-dipole lines perpendicular to strike.

Downhole-to-surface resistivity maps

Detailed delineation of subsurface conductivity distributions often can be accomplished by utilizing drill holes and a combination of surface and downhole electrodes. One such method involves lowering a current electrode down the hole and measuring the voltages on the surface using orthogonal receiving electrode pairs (dipoles). The other current electrode is placed, effectively, at infinity. Quantitative analysis of this configuration has been limited to the case of single spheroidal bodies buried in a uniform half-

space (Merkel and Alexander, 1971; Daniels, 1977). For more comprehensive analysis, it is necessary to include conductive overburden layers, faults, bounded near-surface inhomogeneities, and arbitrary shapes of bodies. The 3-D algorithm developed in this study is ideally suited for downhole studies, since there are no restrictions on the location of current sources or on the definition of any arbitrary conductivity structures.

To illustrate the application of this technique, we have analyzed the downhole-to-surface resistivity array for a simple tabular 3-D body.

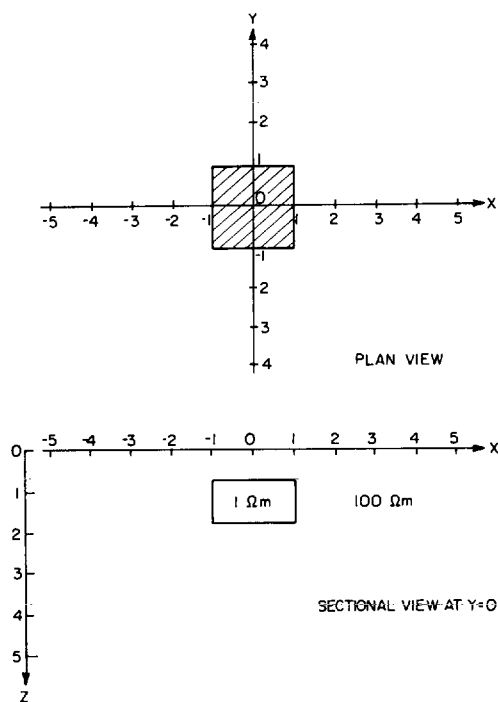The dimensions of this body and the coordinate

FIG. 15. Plan and sectional view of the test model used for the downhole-to-surface electrode configurations.

axes are shown in the plan and sectional views of Figure 15. The resistivity of the tabular body is 1 Ω-m, and that of the surrounding half-space is 100 Ω-m. Maps of apparent resistivity are made using the total electric fields obtained with orthogonal receiver dipoles on the surface. The maps encompass an area of 16 units in the x-direction by 14 units in the y-direction.

Figures 16 a, b, c, and d are the maps of total field apparent resistivities obtained with a current pole located at depths of 0.5, 1.0, 1.5, and 2.0 units, respectively, along a vertical line (drill hole) passing through the center of the body. When the electrode is above the body (Figure 16a), apparent resistivities close to that of the half-space are observed near the hole. Within a radius of 2 units, the values decrease approximately 30 percent. At greater radii, the values return to the half-space resistivity. When the downhole electrode contacts the top of the body (Figure 16b), a pronounced low of 9 Ω-m (L9) is observed over the center of the body. With increasing distance away from the hole, the apparent resistivities increase to the half-space value. For the case of the electrode

within the body (Figure 16c), the central low increases to 23 Ω-m (L23), and the values approach the half-space value within a radius of 3 units. Finally, when the electrode is beneath the body, the central low rises to 68 Ω-m (L68), and a narrow annulus of anomalously high values (120 Ω-m) encloses the surface projection of the body. With increasing radial distance from the hole, the values rapidly approach the surrounding half-space resistivity.

There is usually no difficulty in detecting a body if the drill hole passes through it. A more interesting case, therefore, is that of Figure 17, where the electrode is lowered down a hole located one unit away from the edge of the body ($x = -2, y = 0$). Figures 17 a, b, c, and d are the maps of total field apparent resistivities for an electrode buried at depths of 0.5, 1.0, 1.5, and 2.5 units, respectively. In all of these maps, a localized apparent resistivity high is observed in the vicinity of the hole. A zone of low values lies above the body opposite the hole. Unlike the previous case, the maximum anomaly is now developed when the electrode is at the depth of the center of the body. The change in the anomaly amplitude and pattern as the current electrode moves from within the body to a point 3 units away from the edge of the body, at a depth of 1.5 units, is shown in Figures 16c, 18a (electrode contacting the left side of the body), and in Figures 17c and 18b, where the electrodes are 1 and 3 units away from the edge of the body, respectively. Even at 3 units distance, the anomaly caused by the body is substantial (an A.I. of approximately 80 percent), and the lateral position is well resolved in all cases. These results suggest that the array may be very useful in delineating conductive bodies missed in a drilling program. In this context, it is important to note that single profiles would not be as diagnostic as the surface maps.

Figures 19 a, b, and c are maps of the total field apparent resistivity over a body of infinite strike-length (in the y-direction). The cross-section and depth of the body and component resistivities are identical to the 3-D model used in the previous studies (Figure 15). The depths and locations of the current electrode are identical to those used in constructing the maps of Figures 16a, 16b, and 17c, respectively.

When the electrode is located centrally and above the body (Figure 19a), the anomaly pattern is considerably different from that observed over the 3-D body (Figure 16a). The apparent resistivity values are lower over the entire map area and, in fact, only reach the minimum value of 22 Ω-m (L22) at a radial

APPARENT RESISTIVITY

APPARENT RESISTIVITY

(a)

(b)

APPARENT RESISTIVITY

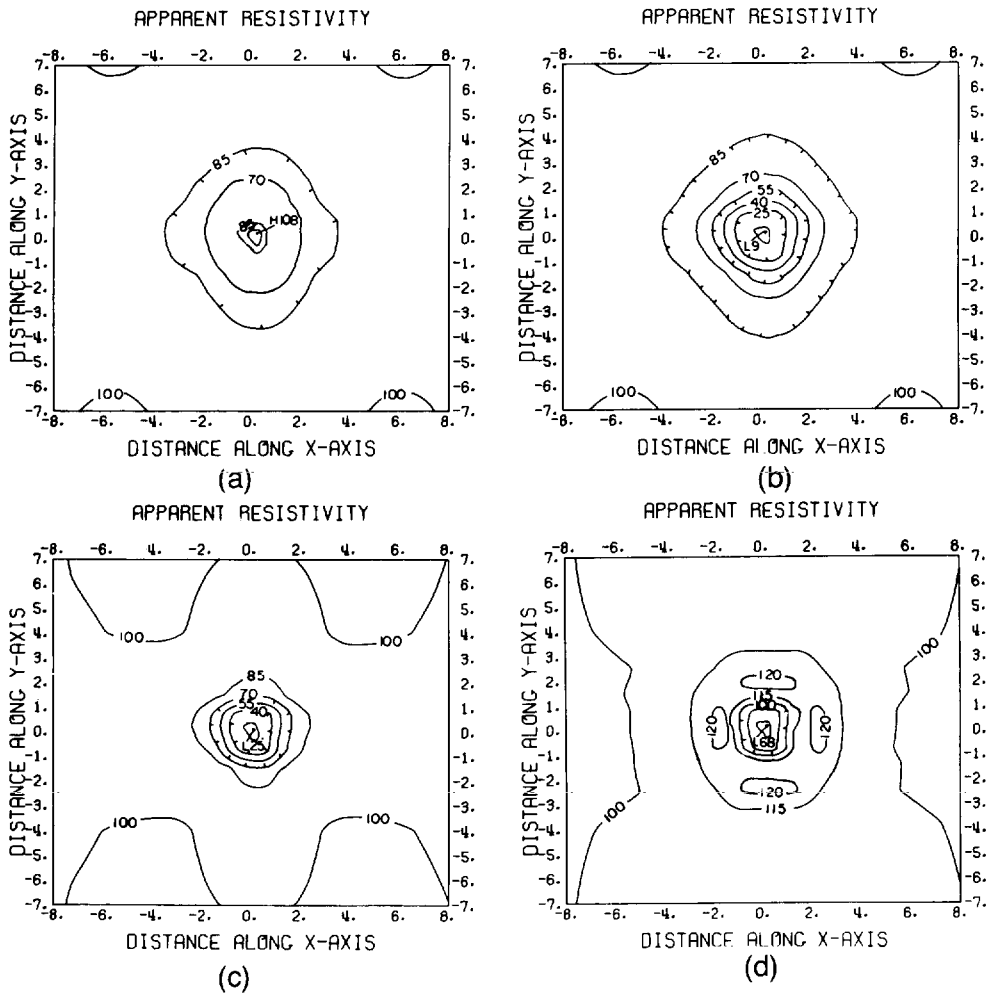APPARENT RESISTIVITY

(c)

(d)

FIG. 16. Maps of total field apparent resistivities with the current pole located along the vertical axis of the test model at depths of (a) 0.5 unit, (b) 1.0 unit, (c) 1.5 units, and (d) 2.5 units below the surface.

distance of 4 units from the hole along strike. As in the 3-D case, the maximum anomaly is produced when the electrode contacts the upper surface of the body (Figure 19b). In both Figures 19a and 19b, the contours show the elongation in the y-direction and, in contrast to the 3-D case, the half-space value is not approached near the edge of the map.

When the electrode is located 1 unit away from the edge of the body and at a depth of 1.5 units (where the maximum anomaly occurs), the 2-D body produces an apparent resistivity map (Figure 19c) quite distinct from the map of the corresponding 3-D model

(Figure 17c). In the 2-D case, an elongated low resistivity zone appears offset from the body on the side away from the current electrode. Surrounding half-space resistivities are not approached within the confines of the map. In both cases, a resistivity high occurs in the vicinity of the hole.

Ambiguities could arise between the anomalies produced by a uniform horizontal layer and those from a 3-D body for a single hole through its center. This ambiguity is removed by data from a second hole. In this context, mise-à-la-masse surveys are best conducted with an electrode located off the axis
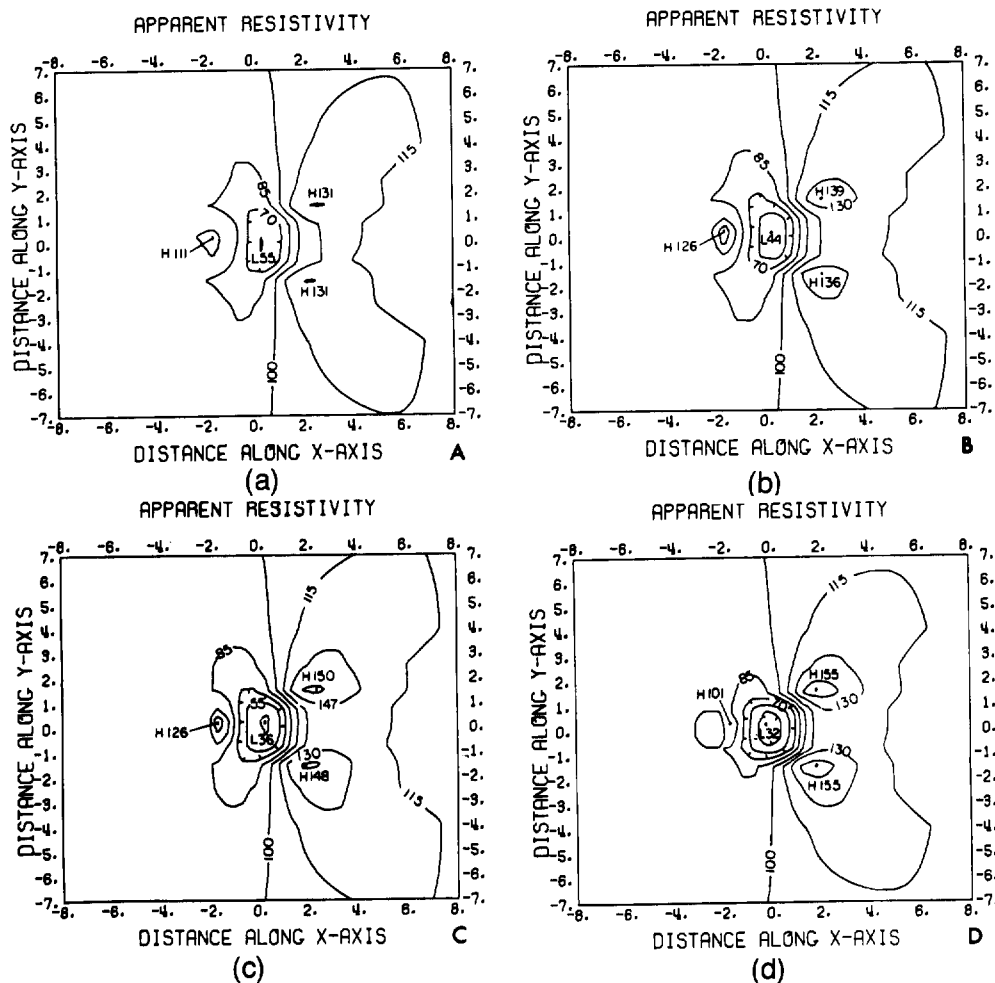
FIG. 17. Maps of total field apparent resistivities with the current pole located 1.0 units away from the edge of the test model at depths of (a) 0.5 unit, (b) 1.0 unit, (c) 1.5 units, and (d) 2.5 units below the surface.

of symmetry. Moreover, the largest anomalies are produced when the electrode is in contact with the top or sides of the body rather than within the body.

CONCLUSIONS

A general algorithm to simulate the response of an arbitrary 3-D resistivity distribution to arbitrary arrays of current and receiver electrodes has been developed. We have illustrated the application of this algorithm with several simple models using both surface and downhole arrays. The finite-difference mesh describing the conductive half-space and the boundary conditions used make the algorithm easily

amenable to the simulation of irregular topography. In addition, the apparent induced-polarization response may be obtained by assigning the intrinsic percent-frequency effect to the resistivity of each elemental volume in the discretization process. Finally, the magnetometric resistivity response may be calculated since the current flow in the lower space is derivable from the potentials at the nodes and the specified conductivities.

ACKNOWLEDGMENTS

APPARENT RESISTIVITY

(a)

APPARENT RESISTIVITY

(a)

APPARENT RESISTIVITY

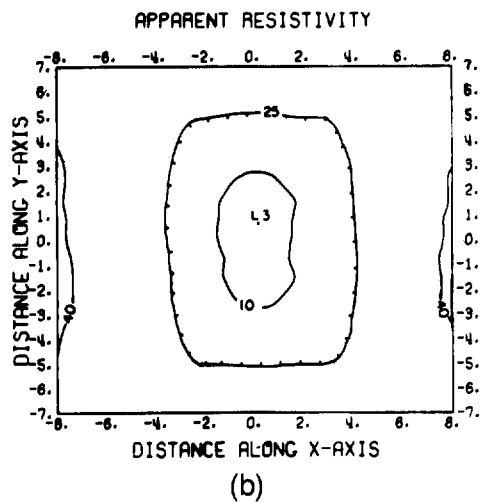(b)

APPARENT RESISTIVITY

(b)
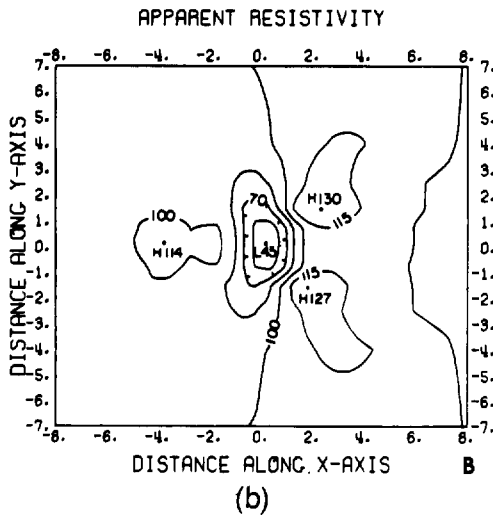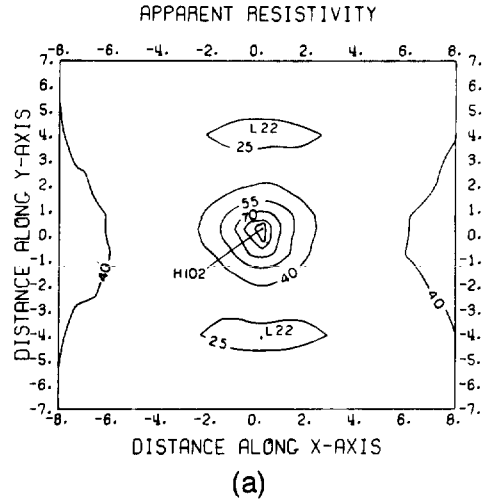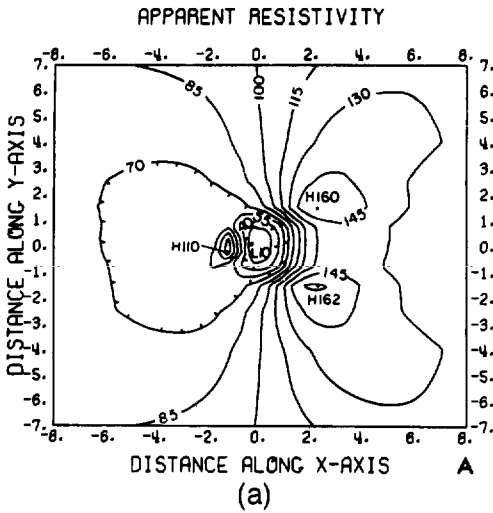
FIG. 18. Maps of total field apparent resistivities with the current pole located at a depth of 1.5 units, and (a) 0.5 units ($x = -1$, $y = 0$) and (b) 3.0 units ($x = -4$, $y = 0$) away from the edge of the test model.
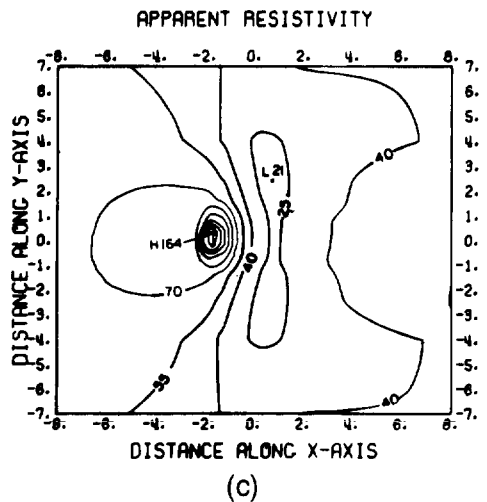
APPARENT RESISTIVITY

(c)

FIG. 19. Maps of total field apparent resistivities over the test model with infinite strike-length in the y-direction with the current pole located along the vertical axis at depth of (a) 0.5 unit, (b) 1.0 units, and (c) with the current pole located 1.0 units away ($x = -2$, $y = 0$) from the edge of the body at a depth of 1.5 units.

for this research has been provided by the U.S. Energy Research and Development Administration through Lawrence Berkeley Laboratory.

REFERENCES

Bakbak, M. R., 1977, Three-dimensional numerical modeling in resistivity prospecting: Ph.D. thesis, University of California, Berkeley.

Coggon, J. H., 1971, Electromagnetic and electrical modeling by the finite element method: Geophysics, v. 36, p. 132.

Concus, P., and Golub, G. H., 1973, Use of fast direct methods for the efficient numerical solution of nonreparable elliptic equations: SIAM, J. Numer. Anal., v. 10, p. 1103.

Daniels, J. J., 1977, Three-dimensional resistivity and induced polarization modeling using buried electrodes: Geophysics, v. 42, p. 1006.

Dey, A., and Morrison, H. F., 1976, Resistivity modeling for arbitrarily shaped two-dimensional structures, Part I: Theoretical formulation: Lawrence Berkeley lab. rep. no. LBL-5223.

Dieter, K., Paterson, N. R., and Grant, F. S., 1969, IP and resistivity type curves for three-dimensional bodies: Geophysics, v. 34, p. 615.

Douglas, J., Jr., and Rachford, H. H., Jr., 1956, On the numerical solution of heat conduction problems in two or three space variables: Trans. Amer. Math. Soc., v. 82, p. 421.

George, A., and Liu, J. W. H., 1976, An automatic nested dissection algorithm for irregular finite element problems: Res. rep. CS-76-38, University of Waterloo, Canada.

Gunn, J. E., 1964, The numerical solution of $\Delta \cdot a\Delta u = f$ by a semiexplicit alternating direction iterative method: Numer. Math., v. 6, p. 181.

Hestenes, M. R., and Stiefel, R., 1952, Method of conjugate gradients for solving linear systems: NBS, J. Res., v. 49, p. 409.

Hohmann, G. W., 1975, Three-dimensional induced polarization and electromagnetic modeling: Geophysics, v. 40, p. 309.

Jepsen, A. F., 1969, Numerical modeling in resistivity prospecting: Ph.D. thesis, University of California, Berkeley.

Kershaw, D. S., 1977, The incomplete Cholesky-conjugate gradient method for the iterative solution of systems of linear equations: Lawrence Livermore Laboratory rep. no. UERL-78333.

Lee, T., 1975, An integral equation and its solution for some two- and three-dimensional problems in resistivity and induced polarization: Geophys. J. R. Astr. Soc., v. 42, p. 81.

McPhar Geophysics, 1966, Catalogue of resistivity and IP model data: McPhar Geophysics, Ltd., Ontario, Canada.

Madden, T. R., 1967, Calculations of induced polarization anomalies for arbitrary two-dimensional resistivity structure: Presented at symposium on IP, University of California, Berkeley.

Meijerink, J. A., and van der Vorst, H. A., 1976, An iterative solution method for linear systems of which the coefficient matrix is a symmetric **M**-matrix: Tech. rep. TR-1, Academic Computer Center, Budapestlaan 6, de Uithof-Utrecht, The Netherlands.

Merkel, R. H., and Alexander, S. S., 1971, Resistivity analysis for models of a sphere in a half-space with buried current sources: Geophys. Prosp., v. 19, p. 640.

Meyer, W. H., 1977, Computer modeling of electromagnetic prospecting methods: Ph.D. thesis, University of California, Berkeley.

Mufti, I. R., 1976, Finite-difference resistivity modeling for arbitrarily shaped two-dimensional structures: Geophysics, v. 41, p. 62.

Reid, J. K., 1972, Two FORTRAN subroutines for direct solution of linear equations whose matrix is sparse, symmetric and positive-definite: UKAEA res. group rep. AERE-R7119.

———— 1976, Sparse matrices: UKAEA computer science and system division rep. no. CSS.31.

Sherman, A. H., 1975, Yale sparse matrix packages: Lawrence Livermore Lab. report no. UCID-30114.

Southwell, R. V., 1946, Relaxation methods in theoretical physics: v. 1, Oxford, Clarendon Press.

Varga, R. S., 1962, Matrix iterative analysis: Engleside Cliffs, N.J. Prentice-Hall.

Wilson, E. L., Klaus-Jurgen, B., and Doherty, W. P., 1974, Direct solution of large systems of linear equations: Computers and Structures, v. 4, p. 363.

Young, D., 1954, Iterative methods for solving partial differential equations of elliptic type: Trans. Am. Math. Soc., v. 76, p. 92.

Zienkiewicz, O. Z., 1971, Finite element method in structural and continuous mechanics: London, McGraw-Hill.